Swarming in Bounded Domains

by

Andrea Thatcher

A Dissertation Presented in Partial Fulfillment
of the Requirements for the Degree
Doctor of Philosophy

Approved November 2015 by the
Graduate Supervisory Committee:

Hans Armbruster, Chair
Sébastien Motsch
Christian Ringhofer
Carl Gardner
Rodrigo Platte

ARIZONA STATE UNIVERSITY

December 2015

ABSTRACT

Swarms of animals, fish, birds, locusts etc. are a common occurrence but their coherence and method of organization poses a major question for mathematics and biology. The Vicsek and the Attraction-Repulsion are two models that have been proposed to explain the emergence of collective motion. A major issue for the Vicsek Model is that its particles are not attracted to each other, leaving the swarm with alignment in velocity but without spatial coherence. Restricting the particles to a bounded domain generates global spatial coherence of swarms while maintaining velocity alignment. While individual particles are specularly reflected at the boundary, the swarm as a whole is not. As a result, new dynamical swarming solutions are found.

The Attraction-Repulsion Model set with a long-range attraction and short-range repulsion interaction potential typically stabilizes to a well-studied flock steady state solution. The particles for a flock remain spatially coherent but have no spatial bound and explore all space. A bounded domain with specularly reflecting walls traps the particles within a specific region. A fundamental refraction law for a swarm impacting on a planar boundary is derived. The swarm reflection varies from specular for a swarm dominated by kinetic energy to inelastic for a swarm dominated by potential energy. Inelastic collisions lead to alignment with the wall and to damped pulsating oscillations of the swarm. The fundamental refraction law provides a one-dimensional iterative map that allows for a prediction and analysis of the trajectory of the center of mass of a flock in a channel and a square domain.

The extension of the wall collisions to a scattering experiment is conducted by setting two identical flocks to collide. The two particle dynamics is studied analytically and shows a transition from scattering: diverging flocks to bound states in the form of oscillations or parallel motions. Numerical studies of collisions of flocks show the same transition where the bound states become either a single translating flock or a rotating (mill) solution.

ACKNOWLEDGMENTS

I consider it an honor to have worked with my advisor, Dr. Armbruster, and express my gratitude for the encouragement, invaluable intuition, and enthusiastic approach to any problem. Thank you for your help and for your extremely challenging yet rewarding classes. Both prove crucial to this dissertation.

I am lucky to have such a great group of people to share in my academic life. Professors Armbruster, Ringhofer, and Motsch along with Dan, I enjoy learning from your own interests and mathematical experiences. My research ideas are a product of your insightful comments and intriguing questions. I extend this list and send a special thanks to my committee members, professors Gardner and Platte, and to Dr. Martin for their suggestions and discussions.

Lastly, to those I love, your constant support through all the angst and anxiety of graduate school makes this dissertation possible. Thank you for listening, offering me advice and being there when I needed a friend. I know that you always believed in me.

TABLE OF CONTENTS

CHAPTER Page

LIST OF FIGURES

Figure Page

Figure Page

Figure Page

Chapter 1

INTRODUCTION

1.1 Overview

Inspired by observing collective motion among a vast spectrum of organisms, experimentalists from several disciplines seek to understand the underlying properties governing the coordinated movement and theoretically develop models capturing such motion and aggregation.

Taking on this challenge, applied mathematicians and physicists for the past few decades have introduced individual-based models (IBM) where particles represent organisms and evolve according to behavioral rules. A specific class of IBM models are self-propelled particle (SPP) models where individual particles are without guidance of a central control or any other external stimuli. Instead, individual particles perceive the behavior of neighbors and adjust their behavior to them. Thus, without the presence of a leader, the particle system evolves according to the position of each particle, which is a function of its neighbors' states.

Originally proposed by Vicsek *et al.* (1995), the Vicsek Model introduces a simple discrete-time model where particles interact by aligning their velocity vector with neighboring particles subject to added noise. Collective behavior is, in this case, characterized not by any direct spatial coherence but by a common direction of motion measured by an observable called *polarization*. As discussed by Vicsek *et al.* (1995), the particles disperse (perhaps not evenly) in space.

However, it is a common experience that most swarms moving in real space show spatial coherence for security reasons as discussed by Handegard *et al.* (2012) and Lin and

Abaid (2013) or directly resulting from the organisms' kinetic motions by Katz *et al.* (2011) and Herbert-Read *et al.* (2011). Hence, to overcome the deficiency of the Vicsek Model, Grégoire and Chaté (2004) and Chaté *et al.* (2008) both introduce an attraction term, adding complications to the model.

In the first part of this thesis, we show that swarms following the basic alignment rules as in the Vicsek Model have spatial coherence when confined within a bounded domain. This spatial coherence does not require additional attraction forces and keeps the Vicsek Model simple.

Taking a cue from atomic physics and Morse potentials, the Attraction-Repulsion Model was developed by D'Orsogna *et al.* (2006). It is a second order SPP model with an interaction pairwise potential that contains parameters that alter the strength and length of the attraction and repulsion forces. Under the conditions concluded by Mogilner *et al.* (2003), the Attraction-Repulsion Model generally converges to a common velocity and the domain of the group is uniformly bounded with a common distance between particles. Complex collective behavior is seen in this model: particles aggregate in a cohesive structure and travel in a like direction (flock), particles rotate within the cohesive structure (rigid-body rotating), or rotate about an empty core (milling and double milling).

Extending the atomic physics analogy a bit further in the second part of this thesis, we study the scattering interaction between flocks in potentials generated by the Attraction-Repulsion Model. Since a flock is a well-defined translational steady state and all particles follow an interaction potential, the collision between a flock and a boundary or between two flocks can be treated as (quasi)-particle scattering.

Such scattering results in internal excitations of the flocks in the former case and in bound states for the latter. We extend this approach to multiple scattering by characterizing the motion of a flock in boxes and channels for the the Attraction-Repulsion Model.

1.2 Literature Review

1.2.1 Models

With the goal of providing a minimal mathematical model that captures complex collective configurations and is amenable to mathematical analysis, the simplest mathematical models represent particles that independently follow the so-called 3-zone model introduced by Reynolds (1987): Individuals remain close to neighbors by moving towards the average position (attraction), individuals move in the same direction as neighbors by moving towards the average heading (alignment), and individuals avoid collisions with neighbors by moving to avoid crowding (Repulsion).

Exploring different variations of the 3-zone model are the papers by Aoki (1982), Couzin *et al.* (2002), Hemelrijk and Kunz (2005), Huth and Wissel (1992), and Reynolds (1987). Seeking to establish conditions under which a group reacts as a whole, Aoki (1982) finds that while attraction and repulsion form groups of individuals, alignment is necessary to maintain the global group cohesion.

The first to simulate swarming behavior is Reynolds (1987). The author develops and implements a method designed initially to mimic bird flocking. The method is based on the three interaction zones and includes a blind zone to model limited peripheral vision (introduced initially in Aoki (1982)). Simulations include barriers where the flock uses a banking mechanism to maneuver around these objects. Exceeding expectations, this model has also contributed to imitating other collective animal behavior and has been used in Disney animation movies (e.g. Lion King).

Huth and Wissel (1992) demonstrate that an 'averaging process' where individuals average over neighbor influences, creates more realistic behavior than a 'decision making process' where an individual determines to interact with a single nearest neighbor. Con-

tradicting conclusions by Aoki (1982), Huth and Wissel find that removing the alignment zone has minor to no effect on the group.

Continuing related work, Couzin *et al.* (2002) study how the width of each interaction zone affects the collective behavior of the system. In particular, altering the size of the attraction and repulsion zone, the authors find sharp transitions between four collective behaviors: swarm where individuals perform attraction-repulsion behavior but have little parallel orientation, torus where particles rotate about an empty core (milling), dynamic parallel group where particles travel in the same direction, and highly parallel group where particles organize into a highly aligned arrangement. To discriminate between these dynamical states, the authors add *angular momentum* to the list of observables.

With the idea of finding a minimal model mimicking collective behavior, Vicsek *et al.* (1995) drop the attraction and repulsion zones and only consider the alignment zone. Particles within the Vicsek Model are scaled to move at a constant speed with their individual headings adopting the average direction of neighboring particles within a finite distance R. Perturbation controlled by a noise term is also added to the model since the alignment in nature is not perfect and individuals make errors. The emergence of collective motion is seen as particles adopt a like heading and move in the same direction. The added noise term forces a smooth phase transition where particles no longer move in the same direction but move in a random fashion. The paper by Czirók *et al.* (1999) further analyzes this model as a one-dimensional representation.

Choosing to build on the Vicsek Model, Cucker and Smale (2007) propose the so-called C-S model which extends the influence horizon of the particles. All particles in the C-S Model see the entire group and the particle velocities are determined by a distance-decaying function. No noise term is included in this model and particles move with arbitrary speed. The C-S Model exhibits collective motion in a sense that the domain of the group is uniformly bounded and the particles approach the common velocity. Variations of the C-S

model include Cucker and Mordecki (2008) and Ha *et al.* (2009) who study the C-S model with an additional considered noise factor and Motsch and Tadmor (2011) who break the permutation symmetry in the C-S model arguing that some agents are more influential than others, thus creating models for swarms with leaders.

As an alternate route of zonal analysis, Mikhailov and Zanette (1999) drop both repulsion and alignment and consider a dynamic model where only a long-range attraction zone is applied in the presence of noise. They discover that the states of the model are either coherently traveling or incoherently oscillating where the translational motion of the swarm is absent. Their conclusions indicate that an increase in noise intensity leads to an abrupt transition from the coherent to the oscillatory state.

A similar model based on an attraction only zone with a presence of noise is studied by Strömbom (2011). Three generated phases are analyzed in this model: Swarm where particles have low and varying alignment, undirected mills and moving aligned groups where particles move in a highly aligned manner. Each phase is characterized by measuring alignment and the area of the smallest square containing the group. By introducing a blindzone to the model, the author observes a dramatic change in patterns: undirected mills become directed and so-called rotating chains appear. For the rotating chains patterns, particles move on an elongated closed curve with zero, one, or two proper self-intersections.

Researchers that argue for two zones as the minimal requirement for mimicking collective motion include Mogilner *et al.* (2003) who study the conditions for a stable, well-spaced swarm to form under the influence of attraction and repulsion forces in a first order model. They find that the range of attraction must be larger than the range of repulsion and the strength of repulsion must be stronger than the strength of attraction. Gazi and Passino (2002, 2004) extend this work by studying an individual-based continuum model with long-range attraction and short-range repulsion.

A second order SPP model, developed in D'Orsogna *et al.* (2006), which we call the Attraction-Repulsion Model, introduces inertia and uses a interaction potential parametrized by the strength and length of the attraction and repulsion forces. We will discuss the Attraction-Repulsion Model in detail in section 2.2. Variations of the attraction-repulsion models were studied by Bazazi *et al.* (2010) and Romanczuk and Schimansky-Geier (2012).

1.2.2 Data

Most of the models discussed in the previous section produce patterns that resemble collective motion observed in nature. However, there are few studies comparing empirical data and models for the dynamical structure of these animal swarms. With the advancement of technology in digital imaging, the study of collective motion in the field and in controlled laboratory experiments can bridge the gap between numerical data and real data. Below, we present examples where some researchers present discoveries and we further discuss conflicting conclusions for various models. Finding observables that best define the overall development of collective motion is still under investigation. Each paper defines its own method and observation with no clear, universal questions or goals.

One of the best known studies has been done by a large group of scientists in Rome (StarFlag project Cavagna *et al.* (2008a,b,c)). They find that interaction among starlings is not based on Euclidean distance (as assumed in almost all models) but based on the topological arrangement of neighboring starlings independent of the density of the flock, i.e. each bird interacts maximally with 6 or 7 neighbors independent of their distance. Ballerini *et al.* (2008) suggest that individuals interact by topological rules rather than a metric distance. However, Bode *et al.* (2010) and Sumpter *et al.* (2012) observe that a local model where individuals interact with neighbors proportional to the inverse of the distance between them produces the same topological arrangement.

Further contradicting the topological distance findings, Lukeman *et al.* (2010) provide a two dimensional mathematical model matching data for the organization and movement of surf scoters off the coast of Alaska. Lukeman *et al.* (2010) describe the type of interaction forces that provide sufficient support to verify spatial patterns. They conclude that interacting surf scoters can be represented by metric zonal models with specific interaction rules applied.

In addition to birds, insects also provide an aggregate motion among species. Bazazi *et al.* (2010) study the motion of locusts commonly known as Mormon crickets located in western North America. The mechanism here that introduces collective behavior is the risk of cannibalism. To reduce the risk of being attacked, the locusts align velocities and move in a common direction.

Along the same lines, Buhl *et al.* (2006, 2012) study desert locusts and find that the marching behavior depends heavily on the density of the locusts and show that theres is a transition between disordered to ordered states that follows similarly to Vicsek *et al.* (1995) and they also identify the critical density for coordinated marching.

Midges are being studied in the both the field by Attanasi *et al.* (2014) and in the lab by Kelley and Ouellette (2013). At adulthood, the midge produces a centralized, mating swarm that shows no overall polarization but statistical evidence supports that the swarm exhibits clusters of correlated motion Kelley and Ouellette (2013). Kelley and Ouellette (2013) provide further details by characterizing the shape of the potential wells keeping the individuals bounded together.

Fish are commonly studied within controlled laboratories. Focusing on local interaction, Katz *et al.* (2011) and Herbert-Read *et al.* (2011) analyze correlations between relative positions and velocities of neighbors to a focal fish, in terms of changing direction and speed. In particular, they develop effective forces that allow fish to form and maintain group structure. The behavioral rules for their data analysis find that the focal fish's

motion turns towards neighbors and avoids collisions by changing speed in the paper by Herbert-Read *et al.* (2011). Katz *et al.* (2011) conclude that speed modulation from both behind and in front of the focal fish acts as an 'alignment rule' and explicitly introducing alignment only modulates the strength of the speed regulation Vicsek and Zafeiris (2012). Alignment will not be a force itself.

Considering fish swimming freely in a tank, Gautrais *et al.* (2009) provide data that describes fish motion via a turning speed and its auto-correlation developing a persistent turning walker model. They illustrate how interactions among fish can be added to this model by quantifying how the turning speed changes for an isolated fish interacting with tank walls and they reproduce characteristics of the fish trajectories. Degond and Motsch (2008b) analytically develop this model further.

Zienkiewicz *et al.* (2014) and Mwaffo *et al.* (2015) study zebrafish in confined environments. Using the data captured from the zebrafish, the authors Zienkiewicz *et al.* (2014) use a purely data-driven approach to provide a modeling framework that fits the quantitative investigation of individuals. Among the investigations is an analysis of simulated trajectories of the model that describe the salient features of the zebrafish, including the wall-following behavior with certain set parameters. This results relates to wall-following behavior we discuss for the Vicsek Model set in a disk and square domain (Chapter 3).

Handegard *et al.* (2012) and Lin and Abaid (2013) extend the analysis of swarms to include predator-prey relationship between a schooling fish prey and their predators.

Data mining and data analysis techniques are used to reduce the dynamic dimensionality of the collective motion. Algorithms such as Isomap developed by Tenenbaum *et al.* (2000). DeLellis *et al.* (2014) are able to identify and interpret different types of collective behavior in five social animal species. As an extension to this study, Gajamannage *et al.* (2015) present a comparable algorithm to Isomap that reduces the dimensionality of the collective motion to find principal manifolds of high-dimensional datasets.

1.2.3 Swams in Bounded Domains

Only a few references directly relate to the focus of our study: We found two papers that study how swarms in the Vicsek Model interact with boundaries: Czirók and Vicsek (2000) study swarming in both a circular and hexagonal domain and find that a rotation of particles develops for high densities and low noise levels. The direction of the rotation is random and creates a single vortex regardless of the system size. Miller and Ouellette (2014) view the animal aggregate as a type of material and test how the three dimensional material breaks apart upon impact with a solid surface. They find that the initial particle mass fragments into smaller particle clusters obeying power-law distributions. In Grossman *et al.* (2008) and Potiguar *et al.* (2014) interactions among *individual* particles is assumed to be inelastic with no other interaction force. In Grossman *et al.* (2008) the particles move in a disk with specularly reflecting boundaries. The model produces collective motion in the sense of vortex formation and swarm migration. The inelastic collisions induce alignment that results in particles adopting like headings. Potiguar *et al.* (2014) establish particle-obstacle interactions with convex rigid obstacles. They find that the particles form a vortex-type motion around the obstacles.

We have found no papers studying the Attraction-Repulsion Model in bounded domains or the scattering of flocks.

1.3 Results

In chapter 3, we analyze how bounded domains affect the swarming behavior of the continuous-time microscopic Vicsek Model proposed by Degond and Motsch (2008a).

As a baseline we study the time evolution of an initially dense group of particles with random initial velocities and observe their swarming motion in $\mathbb{R}^2$. We show that the distribution around the mean position of the particles converges to a Gaussian in two di-

mensions that decays as time increases, confirming the observation that the particles in the Vicsek Model disperse in space Vicsek *et al.* (1995). Altering the domain from free space to periodic domains in $\mathbb{R}^2$, we present and discuss numerical observations and phenomena previously discovered and analyzed by Laurent and Motsch in 2011 Motsch and Navoret (2011) who numerically validated a macroscopic version of the Vicsek Model derived from a large scale limit of the time-continuous Vicsek Model Degond and Motsch (2008a).

Extending this previous work, we consider a channel, aligned and infinitely extended into the vertical direction with vertical walls at $x = 0$ and $x = L$ and periodic boundary conditions in the vertical direction. The walls act as specularly reflecting flat surfaces for individual particles, i.e. the angle of incidence equals the angle of reflection. For the standard parameters of swarming in the Vicsek Model, depending on initial conditions, the swarm has two long-time solutions:

- A stationary flow in the direction of the channel, homogeneous in space that we denote as the *homogeneous flow solution*. Since the flow is essentially parallel to the boundary, the vertical boundaries have little effect on the swarming behavior and the stationary velocity distribution follows the von Mises distribution derived in Motsch and Navoret (2011) for periodic boundary conditions.

- A time dependent solution where the particle flow oscillates between a high density flow upwards at one boundary and a high density flow downwards at the other boundary that we denote as the *shear flow solution*. The shear flow solution is generated by a sticky boundary layer where the particle velocity aligns with the boundary. Particles split into the set that stays in the boundary layer and the swarm that moves between the boundaries. As the swarm moves towards the boundary, particles align with the boundary layer, increase the density in the boundary layer and thus slow down the movement towards the boundary. In section 3.4 we discuss in detail how the flow

towards the boundary reverses and leads to a periodic oscillation. We measure both the period of the oscillation and the width of the boundary layer and show that both increase with the increase in the influence horizon whereas only the boundary layer width increases for increasing noise levels and the period decreases.

Studying swarms in a disk, the typical long term solution becomes a spatially localized swarm that rotates close to the boundary of the disk. When we average the density of the particles over a long time, we find the density profile on the disk is rotationally symmetric and is monotonically increasing towards the boundary of the disk. The density profile is similar to a steady state called the *mill solution* found as a solution to the partial differential equations (PDE) forming the macroscopic Vicsek Model discussed in Motsch and Navoret (2011). In fact, the mill solution is a steady state of the PDE written in polar coordinates in all of $\mathbb{R}^2$ and thus has an infinite total mass. Restricting the mass to a finite value inside the disk, the mill solution becomes indistinguishable from the averaged density of the rotating swarm. Making this identification, we numerically confirm that the mill solution is attracting, an issue that is theoretically proven linearly stable by Degond and Yu (2015). In addition, we generate a conjecture about the relationship between the time averaged dynamics of the swarm motion and the stationary solutions of the macroscopic equations.

Swarms in square domains for a wide range of swarm parameters produce an averaged density profile similar to the circular domain. The associated path of the center of mass of the swarm has a C^4 symmetry in the same way as the swarm in the disk breaks the $O(2)$ symmetry of the disk to an $SO(2)$ symmetry. The trajectory of the center of mass becomes predictable associated with a very well defined periodic behavior of the swarm with high polarization.

Changing swarm parameters, we see that the polarization of the swarm declines and simultaneously the trajectory of the center of mass of the particles becomes unpredictable, eventually leading to Brownian motion of the particles.

In chapter 4, we study the Attraction-Repulsion Model (D'Orsogna *et al.* (2006)). We perform experiments that test how collisions with boundaries alter the flock and test the scattering effects of flocks set to collide.

To generate a fundamental understanding of the wall-flock system, we consider the Attraction-Repulsion Model in an unbounded half space with a reflecting wall set at $x = L$ and allow the flock to impact the wall for various initial trajectories and various potential strengths. Upon impact, the flock experiences a jolt of noise that increases as the potential strength increases and contributes to a loss in the kinetic energy of the system leading to an inelastic collision. In addition, internal elastic oscillations in the swarm are generated. The dominant modes of the oscillations are determined using a Proper Orthogonal Decomposition.

When the flock as a whole collides inelastically with the wall, the stickiness of the wall causes the flock's trajectory to adopt a closer alignment to the wall. We calculate the trajectory of the reflected flock and develop a refraction law as a function of the various initial heading and potential strengths. We find that for smaller potential strengths the flock reflects specularly while for larger potential strength it exhibits a greater alignment to the wall.

Understanding single wall interactions, we study multiple wall interactions within a channel and a square domain by considering iterations of a one-dimensional map based of the derived refraction law and by comparing the results of the iterated map to direct simulations of the flock. For strongly stable equilibria of the map, the trajectories of the iterated map and the direct simulations agree. However, the noise introduced in the flock-wall interaction may change the behavior of the flock qualitatively for weakly stable equilibria. For instance, in a channel domain the typical long-term behavior of both the iterative map and flock converges to a vertical translationally stable motion whose rate of convergence is a function of the potential strength. For smaller potential strengths, the map predicts a

convergence to the vertical heading but the flock is more susceptible to noise and remains in a drifting state for a long time. This noise contribution, however, proves beneficial at larger potential values as the flock quickly leaves the horizontal heading and converges much quicker than the map to the vertical heading.

Similarly, for the square geometry the iterated map predicts a degenerate bifurcation with a continuum of neutrally stable periodic orbits. For high potential strengths (way beyond the bifurcation point), the flock simulation agrees with the iterated map, generating a periodic orbit of the swarm with a C^4 symmetry. Decreasing the strength, the path loses its C^4 symmetry and becomes C^2 symmetric. A further decreased potential strength approaches the bifurcation point and the iterated maps shows an interval of periodic orbits that are neutrally stable. The flock trajectories drift between among these neutrally stable periodic orbits and, in particular, no longer has a preferential rotational direction and often switches rotational direction.

The actual degenerate bifurcation point for the iterated map is characterized by the fact that all points on the map become fixed points, indicating that the flock interacts with the wall specularly and, hence, like in a billiard setting. All initial conditions within this realm lead to a periodic orbit, which are all neutrally stable.

For even weaker potentials the refraction towards the wall is too weak to generate a rotational trajectory. As a result, we find periodic trajectories that are parallel to the boundaries.

To understand the scattering of flocks we examine a pair of interacting particles that are initially set a finite distance apart and directed towards each other. For weak potentials, the two particles continue on their path and diverge, showing a small reduction of the angles between the two paths. At higher strengths, we find two sets of *bound* states: the two particles either converge to a common direction in a slowly damped periodic orbit or

when considering a head on collision, they oscillate back and forth with no net translational motion.

The N particle flocks shows qualitatively the same behavior but results in smoother transitions as the initial angles and potential strength increases. In particular, the oscillatory bound state, is no no longer just limited to initial conditions with no initial y velocity, but are seen for a range of initially small angles with high enough potential strengths. The resulting bound state is the mill solution described previously.

Using the polarization measure, we provide a bifurcation diagram depicting the three regimes of mill, bound translational states and scattering states.

The scattering results agree with the wall-reflection results in the sense that higher potential strength leads to alignment - with the wall or with the other flock whereas small potential strength leads to weak interaction between the wall or the other flock.

1.4 Organization

The outline of this paper is as follows: we introduce three popular SPP Models in Chapter 2. In 3.1, we discuss the simulation setup and difficulties when numerically analyzing the Vicsek Model. In sections 3.2 - 3.5 we produce and examine the numerical results from the Vicsek Model set in various domains. We conclude with a discussion for this chapter in section 3.7.

In 4.1 we setup the simulations of the models and discuss our numerical method approach when numerically analyzing the Attraction-Repulsion Model. In sections 4.2.1 and 4.2.2, we produce and examine the numerical results for the scattering of a flock at walls in various domains. In section 4.2.3, we extract relevant information from the results in section 4.2.1 by performing a Proper Orthogonal Decomposition on the data. We perform collisions of flocks in section 4.3 and conclude this chapter with a discussion in section 4.4.

We finalize our research with concluding remarks and future work in Chapter 5.

Chapter 2

REVIEW OF THE SELF-PROPELLED PARTICLE MODELS

In this chapter, we provide referential review for both the discrete and continuum case of three popular SPP Models: Vicsek, Cucker-Smale, and Attraction-Repulsion. We provide enough detail to give the general idea but refer readers to the herein references for the technicality of each derivation.

2.1 Vicsek Model

The time-discrete Vicsek Model proposed by Vicsek *et al.* (1995) is considered the simplest self-propelled model exhibiting collective motion. Particles in this model are subject to a constant speed and interact by aligning their velocity direction to a local average velocity direction with an addition of noise. The position of each particle in a d-dimensional space is updated by adding the distance traveled during the time step in the direction of its velocity angle.

Specifically, the position of the kth particle at time $t = n$ denoted as x_k^n, $k \in \{1...N\}$, where N is the total number of particles, is updated for each time step Δt as

$$x_k^{n+1} = x_k^n + w_k^n \Delta t. \tag{2.1}$$

Its velocity w_k^n evolves according to the average velocity at each time step $\bar{w}_k^n$ of the neighboring particles along with an addition of noise η_k. Precisely, the velocity update is written as

$$w_k^{n+1} = \bar{w}_k^n + \eta_k; \qquad w_k^{n+1} = \frac{w_k^{n+1}}{|w_k^{n+1}|} \tag{2.2}$$

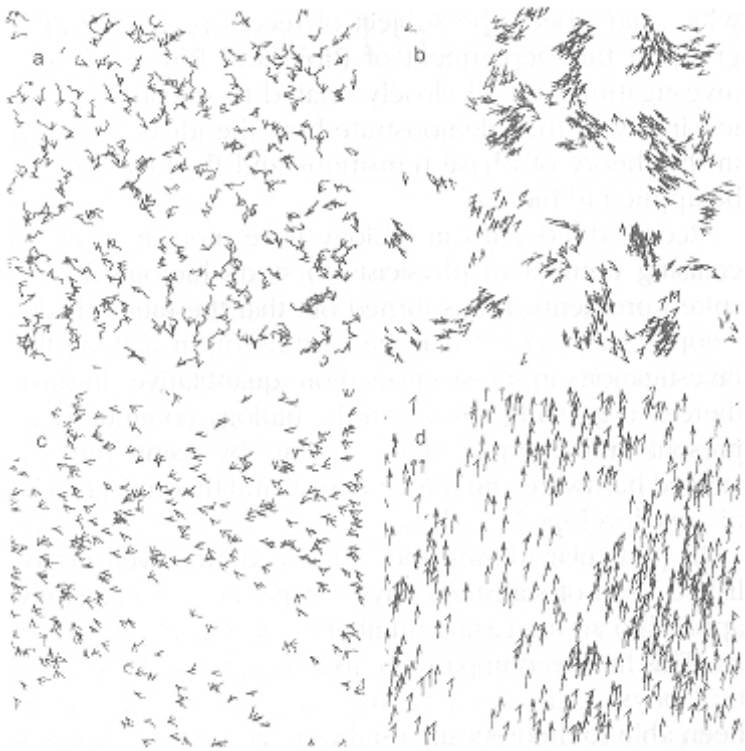

Figure 2.1: Velocity and Particle Distribution for the Vicsek Model Originally Produced by Vicsek *et al.* (1995). (a) Initial state. (b) Small densities and noise: Small groups form and move coherently in random directions. (c) Higher density and noise: The particles move in random direction with some correlation. (d) Higher density and small noise: The motion becomes ordered.

where

$$\bar{w}_k^n = \frac{J_k^n}{|J_k^n|},\ J_k^n = \sum_{j,|x_j^n - x_k^n|<R} w_j^n. \tag{2.3}$$

Notice that the velocity average $\bar{w}_k$ is taken over the neighboring particles to particle k within a radius $R > 0$ ball centered at the position x_k^n. The Vicsek Model assumes a constant speed hence the normalization in Eq.(2.2). The noise $\eta \in \mathbb{R}^d$ is typically assumed to be IDD random variables with uniform distribution in $[-a, a]$, $a > 0$.

Vicsek *et al.* (1995) consider periodic boundary conditions and provide figure 2.1 as typical collective motion in the model. The authors measure the collective nature of the

particles by calculating the average velocity of the system

$$\phi_N = \frac{1}{N}\left|\sum_{k=1}^{N} w_k\right| \tag{2.4}$$

for various noise values η and several number of particles. They show that there is a smooth transition from an ordered state $\phi_N \approx 1$ to disordered state $\phi_N << 1$. The quantity $\phi_N \approx 1$ represents individuals adopting a like heading and $\phi_N << 1$ represents individuals whose headings balance out.

Degond and Motsch (2008a) derive the continuum limit of the model Eq. (2.2)

$$\begin{aligned} \tfrac{dx_k}{dt} =& w_k \\ dw_k =& (\mathbb{I} - w_k \otimes w_k)(\nu \bar{w}_k dt + \sqrt{2d}\, dB_t) \end{aligned} \tag{2.5}$$

where $\mathbb{I}$ is the identity matrix, $\otimes$ is the tensor product of vectors, dB_t is Brownian motion with intensity $\sqrt{2d}$ and $\bar{w}_k$ is the continuous velocity average in a ball of size R equivalent to Eq. (2.3). The operator $(\mathbb{I} - w_k \otimes w_k)$ is the orthogonal projector onto the plane normal to w_k, ensuring that the velocity vector is an element of the unit sphere, $w \in S^n$. The interaction frequency ν and the diffusion coefficient d replace the time step Δt and noise level η. Hence ν^{-1} is the typical decay time for perturbations of particles velocity to align with their neighbors. For analytical convenience a Gaussian distributed noise with intensity $\sqrt{2d}$ is used in place of a uniformly distributed noise.

With this time-continuous model, Motsch and Navoret (2011) rescale (2.5) in both space and time to compare numerical simulations to the macroscopic model derived in Degond and Motsch (2008a). Taking $t = \epsilon t$ and $x = \epsilon x$, system (2.5) becomes by Motsch and Navoret (2011)

$$\begin{aligned} \tfrac{dx_k}{dt} =& w_k \\ dw_k =& \tfrac{1}{\epsilon}(\mathbb{I} - w_k \otimes w_k)(\overline{w}_k dt + \sqrt{2d}\, dB_t) \end{aligned} \tag{2.6}$$

where the primes are dropped for convenience and we set $\nu = 1$. ϵ is the ratio between the macroscopic Vicsek Model and the Vicsek Model Eq. (2.5).

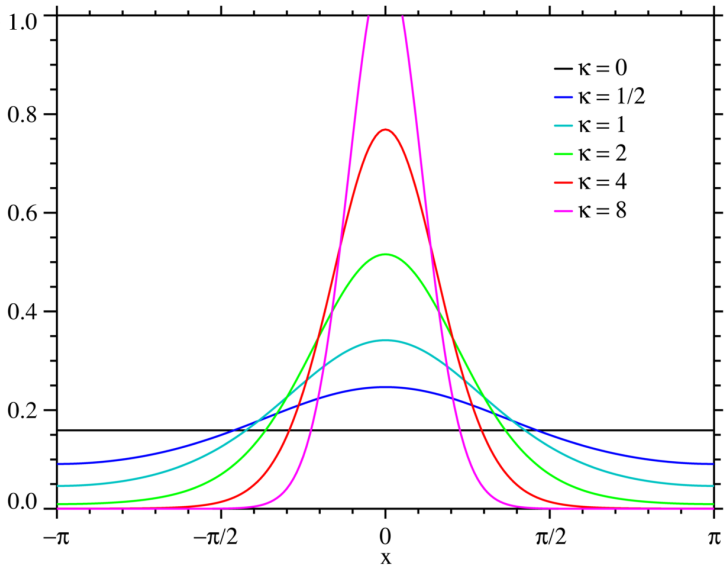

Figure 2.2: The von Mises Distribution Originally Produced by Wikipedia. The velocity variable is defined on the unit circle as $w = e^i x$ where $x \in [-\pi, \pi]$. The parameter $\kappa = \frac{1}{d}$ controls the width of this distribution. When $\kappa = 0$, $d \to \infty$ and the distribution is uniform. As κ increases, d decreases and we see the distribution's width decrease while the height increases. The direction of the Ω corresponds to the center of the peak. Here, the average velocity is $\Omega = [1, 0]$.

When providing the macroscopic representation of the Vicsek Model, Degond and Motsch (2008a) introduce a non-conventional concept of a collisional invariant of a collision operator that operates on functions of w only. The equilibrium solutions of this collisional operator represents the particle velocity distribution for the directions $\omega \in S^1$ which converges to the von Mises distribution

$$M_\Omega(\omega) = Z \exp\left[\frac{\omega \cdot \Omega}{d}\right]. \tag{2.7}$$

Here Ω is the direction of the mean velocity of the particles and Z is a normalizing constant. The graphical representation of Eq. (2.7) is in figure 2.2.

After establishing an equilibrium solution to the collisional operator, the authors are free to derive the macroscopic Vicsek Model. The evolution of the macroscopic Vicsek Model depends on the movement of two macroscopic quantities: the density of the particles ρ and the direction of the particle flow Ω. With these two quantities, the macroscopic Vicsek

Model is written as:

$$\begin{aligned} \partial_t \rho + c_1 \nabla_x \cdot (\rho \Omega) =& 0 \\ \rho(\partial_t \Omega + c_2(\Omega \cdot \nabla)\Omega) + \lambda(\mathbb{I} - \Omega \otimes \Omega)\nabla_x \rho =& 0 \end{aligned} \tag{2.8}$$

where c_1, c_2 and λ are d dependent coefficients provided in Appendix A. We note that $c_1 \neq c_2$ and that the model has the geometric constraint $|\Omega| = 1$. With the additional $\mathbb{I} - \Omega \otimes \Omega$ term, Eq. (2.8) is a nonconservative, hyperbolic system with a geometric constraint, Motsch and Navoret (2011).

The hydrodynamic model is further analyzed by Degond and Yang (2010) where presented are $O(\epsilon)$ corrections to system (2.8) by using the standard Chapman-Enskog theory. Note that ϵ is the ratio between the macroscopic Vicsek Model Eq. (2.8) and the microscopic Vicsek Model Eq. (2.5). Since the system does not conserve momentum and is non-isotropy in fluids (the fluid adopts a common heading), the derivation is not standard and involves added diffusion terms to both the mass and velocity equations.

As an extended application to those introducing attraction-repulsion forces, Degond *et al.* (2011) show that the non-local effects of the alignment and attraction-repulsion can be kept in the hydrodynamic limit by introducing different scaling in the kinetic representation of the continuous-time Vicsek Model with the additional attraction-repulsion interaction potential. They prove the local-in-time existence of solutions for the viscous system in two-dimensions and the inviscid model in three-dimensions. Numerical quantification of this model is not presented but suggested as future work.

Restricting the macroscopic Vicsek Model to a disk domain, Degond and Yu (2015) conduct an analysis on the linearized polar coordinate representation of Eq. (2.8). Presented by Motsch and Navoret (2011), the steady state of the polar coordinate system has a density and velocity profile similar to the mill solution. The steady state is assumed to satisfy all $\mathbb{R}^2$, implying an infinite total mass. The paper proves no analytical support for the stability of this steady state. Degond and Yu (2015), however, show that the perfectly

polarized steady state satisfying the linearized polar coordinate system with an imposed a tangential flow boundary condition has only imaginary modes that form a countable set associated to an orthonormal basis of eigenvectors. The steady state, therefore, is linearly stable.

Performing numerical studies, Motsch and Navoret (2011) and Gamba and Kang (2015) present numerical description for the microscopic, kinetic and macroscopic Vicsek Models. Motsch and Navoret (2011) numerically seek to validate the macroscopic to the microscopic Vicsek Model. Since Eq. (2.8) is a nonconservative, hyperbolic system with a geometric constraint as mentioned above, there is no standard theory to study this model. Deriving the numerical scheme *splitting method*, the authors reveal that the microscopic and macroscopic models are in good agreement, confirming the relevance of the macroscopic Vicsek Model.

Gamba and Kang (2015) provide a different approach by presenting a numerical description for the kinetic representation of the Vicsek Model provided by Degond and Motsch (2008a) and comparing the numerical kinetic model to solutions of the macroscopic and microscopic Vicsek Model. The numerical scheme to represent the macroscopic Vicsek Model is the *splitting method*, previously proposed by Motsch and Navoret (2011). Their results conclude that the kinetic model captures the key aspects of both models such as vortex formation and traveling waves.

2.2 Attraction-Repulsion Model

The Attraction-Repulsion Mode is introduced by D'Orsogna *et al.* (2006). It describes particles that move according to Newton's law in a potential that is attracting for large distances and repelling for short distances:

$$\begin{aligned} \tfrac{dx_i}{dt} &= v_i \\ \tfrac{dv_i}{dt} &= (\alpha - \beta|v_i|^2)v_i - \lambda \nabla_{x_i} \textstyle\sum_{j \neq i} U(x_i - x_j) \end{aligned} \tag{2.9}$$

where $\alpha \geq 0$ is the self-propulsion force and $\beta|v_i|^2 \geq 0$ is a Raleigh type friction force. Carrillo *et al.* (2009) introduce λ as the potential modulator. Here, we refer to λ as the potential pre-factor. The function $U(x)$ is the attraction-repulsion potential given typically as the Morse potential:

$$U(x) = k(|x|), \quad k(r) = -C_a \text{exp}(-r/l_A) + C_R \text{exp}(-r/l_R) \tag{2.10}$$

where C_A, l_A, C_R and l_R are the the strength of typical length of attraction and repulsion, respectively. The potential is chosen such that U is repulsive for small distance r and attractive for large enough r.

We can nondimensionalize Eq. (2.11) as

$$U(x) = k(|x|) \quad , \quad k(r) = C\text{exp}(-r/l) - \text{exp}(-r) \tag{2.11}$$

where $C = C_r/C_a$ and $l = l_R/l_A$. In this paper, we use the nondimensionalized Morse potential to investigate the model.

If we ignore the effects attributed by the Morse potential, the self-acceleration force αv_i and the self-deceleration force $\beta|v_i|^2 v_i$ tend to balance out and the system sustains a constant (nontrivial) speed $|v| = \sqrt{\alpha/\beta}$ which has no influence on the orientation of the velocities. The orientation of the velocities depends on the relationship between C and l.

The terms "H-Stability" and "catastrophic" are properties directly related to the pair-wise potential $U(x)$ in Eq. (2.11) and help to understand what spatial structures can be present for a given parameter choice. H-Stability is seen in typical thermodynamic systems where increasing the number of particles only weakly affects the average interspacing distance between the particles, leading to volume growth of the system. On the other hand, increasing the number of particles in a catastrophic system causes the spacing between particles to reduce, keeping the volume constant.

The phase diagram of how the Morse potential relies on the parameter space C and l is seen below in figure 2.3 with all credit given to D'Orsogna *et al.* (2006).

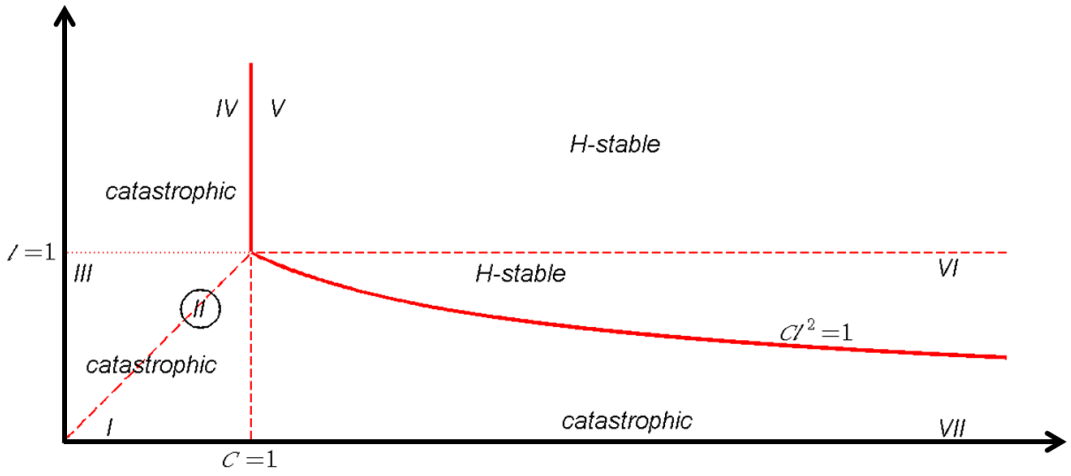

Figure 2.3: Phase Diagram of the Morse Potential Depending on the Parameters (C, l). Figure was originally produced by D'Orsogna *et al.* (2006).

Regions I, II, and III have strong pairwise attraction $C < 1$ and a short active range for repulsion $l < 1$. The equilibrium distance between particles is zero and the particles within this region form coherent clumps that orbit the center of the swarm in Regions I and III. When $N \to \infty$, the clumps lose their coherence and merge in Region III. The intermediate Region II provides patterns where the particles develop rings. As N increases, the ring radius decreases.

Maintaining strong attraction ($C < 1$) and increasing the active range of repulsion ($l > 1$), we enter region IV. Here, the system behaves similarly to Region III if particles are within a certain distance. Those farther away will be repulsed and diverge.

No coherent state is seen when both the repulsion active range and amplitude are greater than the attraction $l > 1$ and $C > 1$ (Region V).

Experiencing short-range repulsion and long-range attraction, Regions VI and VII hold particular interest in our study of swarms. This type of interaction allows the particles to settle and maintain a positive minimal distance from each other.

For $Cl^2 > 1$ (region VI), the Morse Potential (figure 2.4a)) is H-stable. That is, for any arbitrarily large number of agents N, there exists a constant $B \geq 0$ such that

$$\sum_i U(x_i) \geq -NB. \tag{2.12}$$

Thus, particles will not collapse onto themselves and they self-organize with a fixed relative distance from each other. As N grows, the swarm's radius will grow accordingly.

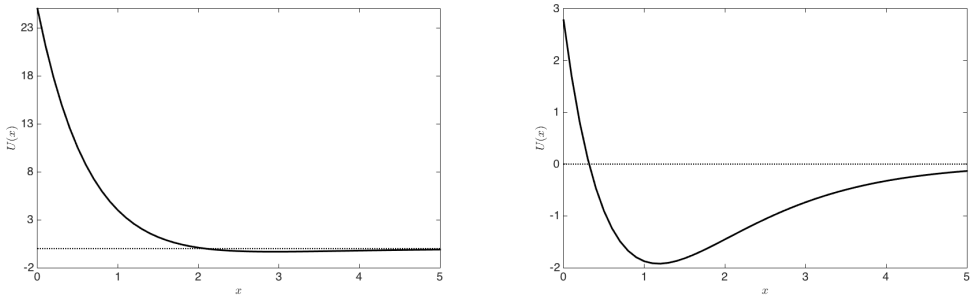

(a) H-Stable: $C = 2, l = 3/4$ (b) Catastrophic: $C = 10/9, l = 3/4$

Figure 2.4: Morse Potential for H-Stable and Catastrophic Regions. a) H-Stable region: $C = 2$ and $l = 3/4$. b) Catastrophic region: $C = 10/9$ and $l = 3/4$.

Structures in Region VI depend on the values of α and β. For larger values of α/β, particles disperse while at relatively low values of α/β, coherent structures form. Depending on initial conditions, patterns seen in this regime are the rigid-body rotation state where the center of mass of the particles is not stationary but moves in a random path (see Figure 2.5b)) or a flock (Figure 2.5a)) where all particles travel with a unified velocity $\sqrt{\alpha/\beta}$. All particles within these two states maintain a minimal relative distance and both are seen when α is small or, more technical, the confining interaction potential is stronger than the kinetic energy of the individual particles as discussed by Chuang *et al.* (2007). Upon increasing α, the particles gain enough kinetic energy to dissolve the aggregation.

With $Cl^2 < 1$ (region VII), the Morse Potential (figure 2.4b)) is catastrophic. The inequality (2.12) does not hold and collapse of particles will occur. Similar to region (VI), larger values of α/β give rise to dispersion and smaller values of α/β create rigid-like

motion. Depending on the initial conditions, flocks and a rigid-body rotation state are also present in this regime with similar characteristics to Region VI. However, the transitional state from the rigid-body rotation for an increasing α differs Chuang *et al.* (2007). When α increases, the interaction potential is still strong enough and a core-free mill state emerges (Figure 2.5c)). Since particles travel at a non-zero uniform speed, the interaction potential is not strong enough to support them too close to the center and an empty core forms. The size of the empty core depends on N. As $N \to \infty$, the empty core core collapses D'Orsogna *et al.* (2006).

Further increasing α, both single and double mills (Figure 2.5d)) are possible states since the interaction potential is not effective enough to change the direction of motion of particles. If a particle is traveling in the opposite direction, it maintains this direction. When the kinetic energy greatly surpasses the strength of the interaction potential, the swarm breaks apart and no aggregation can be found.

The flock solution has a precise analytical definition:

Definition 1. *A flock solution of the particle model (2.9) is a spatial configuration $\hat{x}$ with zero net interaction force on every particle, that translates at a uniform velocity $m_0 \in \mathbb{R}^2$ with $|m_0| = \sqrt{\alpha/\beta}$, hence $(x_i(t), v_i(t)) = (\hat{x}_i + tm_0, m_0)$.*
The spatial configuration $\hat{x}$ is a stationary state to the first-order interacting particle system

$$\frac{dx_i}{dt} = -\sum_{j \neq i} \nabla_i U(x_i - x_j). \tag{2.13}$$

Notice that the flock is not rotationally invariant. A small rotation about the center of mass of the flock still satisfies Eq. (2.13) but has a different spatial representation. Carrillo *et al.* (2014a) provide a stability analysis for this flock solution and show that the flock is capable of withstanding small perturbations.

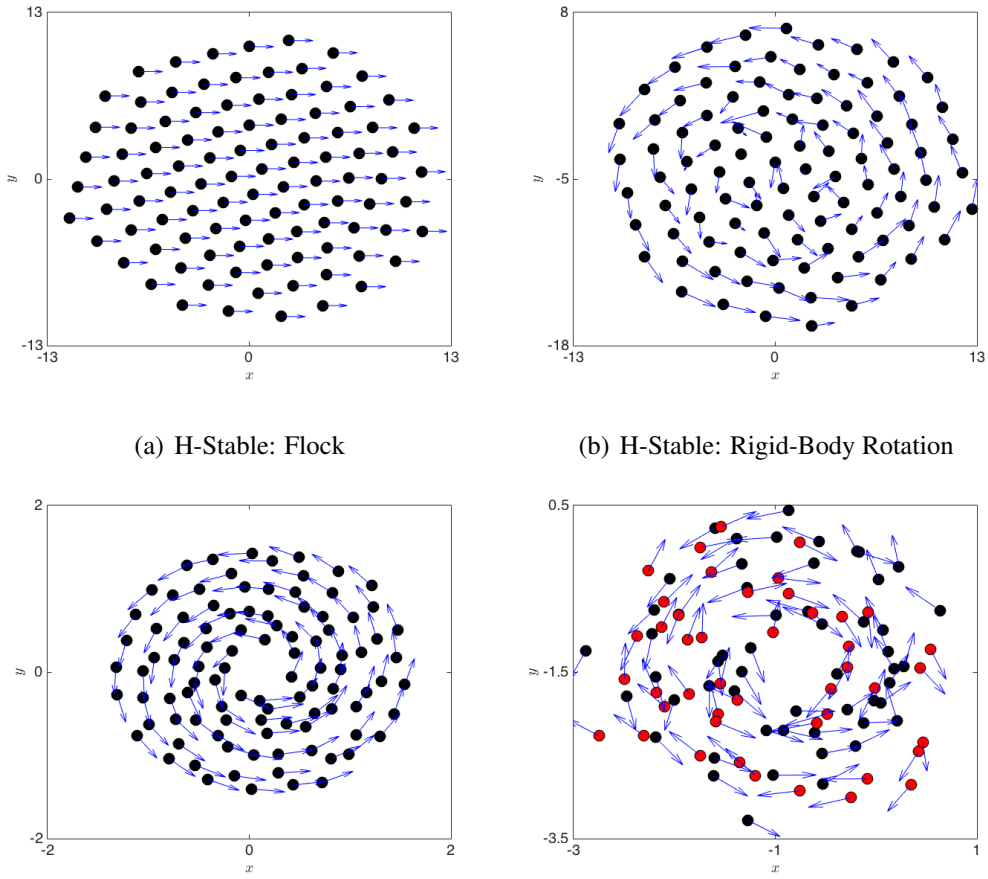

(a) H-Stable: Flock

(b) H-Stable: Rigid-Body Rotation

(c) Catastrophic: Single Mill

(d) Catastrophic: Double Mill

Figure 2.5: Stationary States Seen in H-Stable and Catastrophic Regions. States a) and b) are similarly found in catastrophic region, but states c) and d) are never found in H-Stable region. d) Double milling state: red particles rotate clockwise while black rotate counter clockwise.

Density profiles for single and double milling patterns have been found numerically by Levine *et al.* (2000) and Carrillo *et al.* (2009). Levine *et al.* (2000) develop a continuum version of system (2.9) via coarse grain averaging. Assuming centripetal interaction forces, they find a vortex solution and show an excellent match between the vortex solution and the numerical solution for the particles model. A rigorous proof for the existence centripetal interaction forces is lacking. Carrillo *et al.* (2009) derive macroscopic hydrodynamics equations from kinetic equations. They discuss the single mill density profile in relation to Levine *et al.* (2000) work, but in addition, provide a density solution to the double mill as

superimposed single mills of velocities v, $-v$. The total velocity is zero, however, the two populations coexist, rotate in opposite directions and have a total density exactly equal to the single mill's density profile.

Here, we note that other potentials have been considered such as the quasi-morse potential by Carrillo *et al.* (2013, 2014b) or Log-Newtonian potential by Fetecau *et al.* (2011).

Chapter 3

VICSEK MODEL IN BOUNDED DOMAINS

In this chapter, we show that the swarms generated by the Vicsek Model, if confined within a bounded domain with spectrally reflecting boundaries, have spatial coherence without additional attraction forces. We also find new types of collective motion in addition to the single vortex discussed by Czirók and Vicsek (2000) and analyze their behavior as a function of the noise level and the influence horizon.

3.1 Simulation Setup

We use Euler's method to compute the numerical approximation to system (2.6). For Euler's method to remain stable, we require $\frac{1}{\epsilon}\Delta t < 1$.

When reaching the reflecting boundary, a particle j will experience specular reflection and its velocity is updated

$$V_{\text{new}} = V_{\text{old}} - 2(V_{\text{old}} \cdot \vec{n})\vec{n} \tag{3.1}$$

where $\vec{n}$ is the normal vector to the boundary. After reflecting, we normalize $|V_{\text{new}}| = 1$ for the restriction of the Vicsek Model.

A particle j interacting with the wall at time step $n\Delta t$ will not update its velocity according to Eq. (2.6) until the next time step $(n+1)\Delta t$. That is, we have a time step $(n+\zeta_j)\Delta t$ with $0 < \zeta_j < 1$ where the velocity $w_j^{n+\zeta_j}$ is reflected by Eq. (4.1) and the particle j continues on this new trajectory until time step $n+1$. At this new time step $n+1$, the velocity updates according to Eq. (2.6) with the reflected velocity $w_j^{n+\zeta_j}$ instead of the original velocity w_j^n.

As a result, different time steps satisfying the CFL condition create different transient results. We keep our time step $\Delta t = 0.01$ to avoid conflicting results that depend on the time step.

The parameter choices for each simulation (unless stated otherwise) are: the time step $\Delta t = 0.01$; $\epsilon = 0.1$; the number of particles is $N = 10,000$; and the radius of interaction is $R = 0.5$. Simulations are ran for various lengths of time. Most settled to the described behavior after an order of 100 time units. We ran most tests ten times longer to verify the behavior.

Simulations were run using gfortran on 96gb RAM and 2 Intel(R) Xeon(R) CPU E5-2620 0 @ 2.00GHz processors and took an average of 600 seconds to run 100 time units.

3.2 Swarms in $\mathbb{R}^2$

Degond and Motsch (2008a) use a kinetic representation of the Vicsek Model to derive a macroscopic model in the form of partial differential equations. The derivation is based on the particle velocity distribution for the directions $\omega \in S^1$ converging to the von Mises distribution

$$M_\Omega(\omega) = Z \exp\left[\frac{\omega \cdot \Omega}{d}\right]. \tag{3.2}$$

where Ω is the direction of the mean velocity of the particles and Z is a normalizing constant.

Assuming an initial swarm, localized in space and with a velocity distribution satisfying Eq. (3.2) with $\Omega = [1, 0]$ and a large alignment horizon $R \gg 1$, the velocity in the x-direction becomes

$$\bar{v}_x = \int \cos(w) \exp\left[\frac{\cos(w)}{d}\right] dw, \tag{3.3}$$

decreasing with the noise level d. Since $\omega \in S^1$, as the mean velocity decreases, the width of the distribution in the y-direction increases. The swarm as a whole moves into the x-direction and each particle in the swarm performs an unbiased random walk in the

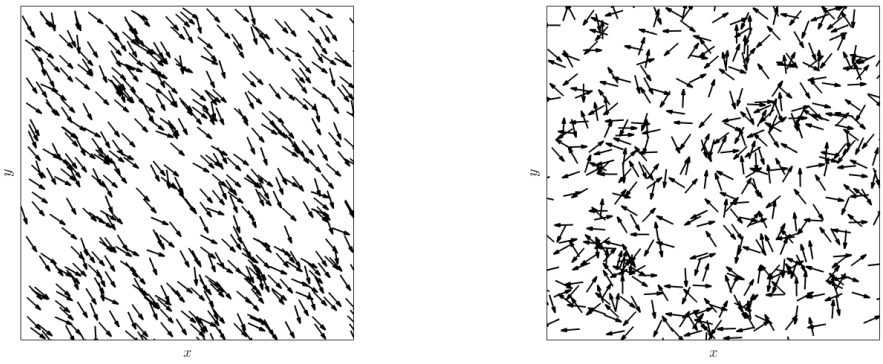

(a) $\phi_N = 0.97389$ (b) $\phi_N = 0.13892$

Figure 3.1: Particle Simulations of Coherent and Random Motion for the Vicsek Model. a) Particles move in a like direction with little variation. b) Particles move randomly.

y-direction and a biased random walk in the x-direction with $\overline{v}_x$. Hence, while the center of mass of the swarm moves according to $\bar{x} = \bar{v}_x(t)t$ and $\bar{y} = 0$, the distribution around the mean position as $t \to \infty$ becomes a Gaussian that decays in time. As a result, the spatial correlations of the particles in the swarm decay to zero, the mass diffuses in space to a low density and the swarm eventually disintegrates.

3.3 Periodic Boundary Conditions

The paper by Motsch and Navoret (2011) numerically compares the microscopic Vicsek Model (Eq. 2.6) and the macroscopic Vicsek Model, showing that the velocity distribution on S^1 converges to the associated von Mises Distribution Eq. (3.2). An easily calculated observable for both models is the average velocity given by

$$\phi_N = \frac{1}{N}\left|\sum_{k=1}^{N} w_k^n\right|, \qquad \phi = \left|\int_\omega \omega M_\Omega(\omega) d\omega\right|. \tag{3.4}$$

$\phi \approx 1$ implies particles behave like a swarm and all move in the same direction and $\phi << 1$ implies the particles move randomly with no ordered motion. Particle representations of both these cases are provided in figure 3.1.

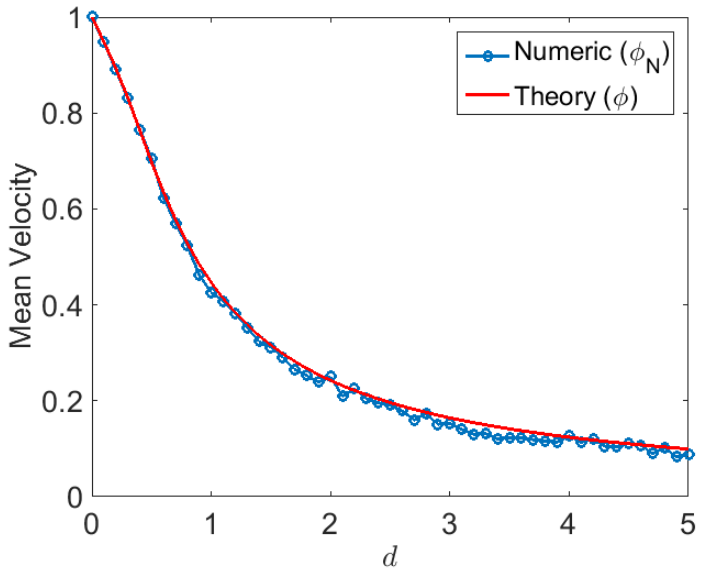

Figure 3.2: Mean Velocities ϕ_N and ϕ (Eq. 3.4) for Varying Noise Levels d for Swarming States with Periodic Boundary Conditions. Number of particles $N = 1000$, box size $L = 1$, and ratio $\epsilon = 1$. R and Δt are set to default. The simulations run for 10 time units with the plotted values being averaged over 10 simulations.

Computing the two average velocities in Eq. (3.4) for varying noise levels d, we see that the particle average velocity ϕ_N matches nicely with the theoretical mean velocity ϕ in figure 3.2. At smaller d, the particles adopt the same heading (see figure 3.1a) with little variation but experiences a smooth transition from an ordered state to a disordered state (see figure 3.1b) as d increases. This type of transition is also seen in the discrete-time Vicsek Model by Vicsek *et al.* (1995).

Note that since the domain becomes bounded (the torus T^2), the Brownian motion generates a uniform distribution in space for both states, the collective movement and the disordered state.

Figure 3.3 shows the mean velocity as a function of the noise levels for increasing domains, keeping the density constant. Motsch and Navoret (2011) find that for large noise levels d the average velocity ϕ_N no longer matches ϕ, the one derived from the von Mises distribution. Conversely, keeping the box fixed and increasing the density of the

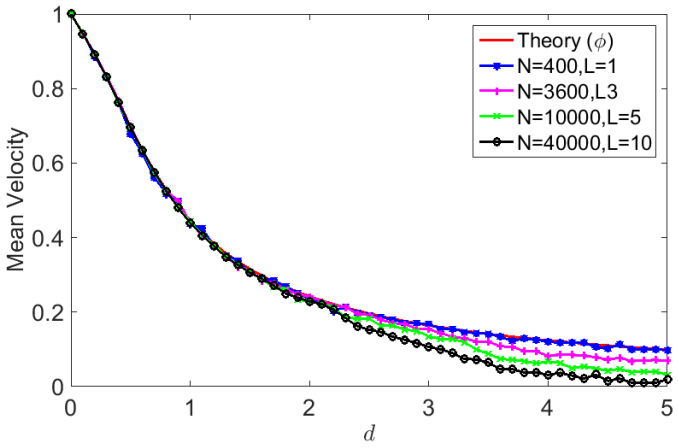

Figure 3.3: Mean Velocities ϕ_N and ϕ (Eq. 3.4) as a Function of the Noise Levels d for Swarming States With Periodic Boundary Conditions. The Average Velocity for the Microscopic Model Depends on the Box Sizes Even Though the Density Remains the Same for All Boxes. Number of particles $N = 400, 3600, 10000,$ and 40000; box size $L = 1$, 3, 5 and 10. ϵ, R and Δt are set to figure 3.2. The simulations run for 100 time units with the plotted values being averaged over 10 simulations.

particles in the box, figure 3.4 shows that the average velocity converges to ϕ confirming the equivalence of the two models as $N \to \infty$.

3.4 Channel Domain

We consider a Vicsek Swarm Model (Eq. 2.6) in a one-dimensional channel with x as the transverse direction and y as the parallel direction, assuming specular reflection for the individual particles at the vertical boundaries at $x = 0$ and $x = L$. We set up the simulations for this section as a Riemann problem assuming a uniformly distributed density ρ and initial swarm directions that differ for the right and left half of the channel. The initial velocities for each particle w_k are set according to the Von Mises distribution Eq. (3.2) with $d = 0.02$ (for the initial distribution only). In the left half of the channel, i.e for positions $0 \leq x < L/2$ the mean direction of the velocity is given by $\Omega_L = (\cos\theta_0, \sin\theta_0)$, in the right half of the channel, i.e. for positions $L/2 < x \leq L$ the mean direction is $\Omega_R = (\cos\theta_0, \text{-}\sin\theta_0)$. Figure 3.5 shows an example of this initial velocity distribution.

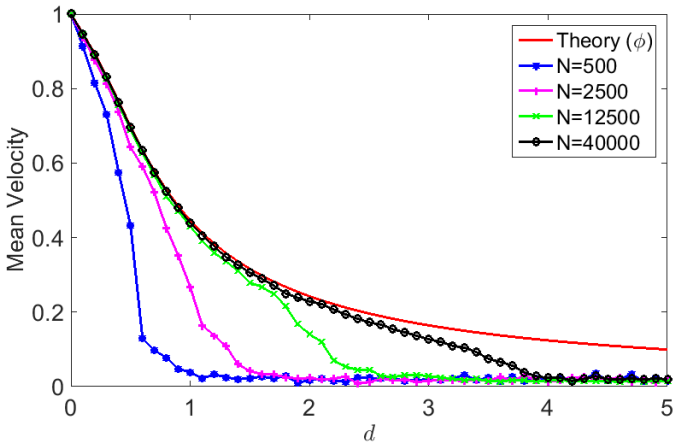

Figure 3.4: Mean velocities ϕ_N and ϕ (Eq. 3.4) as a Function of the Noise Levels d for Swarming States with Periodic Boundary Conditions. For a Fixed Box Size, the Mean Velocity Approaches the Macroscopic Mean Velocity as the Density of the Swarm Increases. Number of particles $N = 500, 2500, 12500,$ and 40000; box size $L = 10$. ϵ, R and Δt are set to figure 3.2. The simulations run for 100 time units with the plotted values being averaged over 10 simulations.

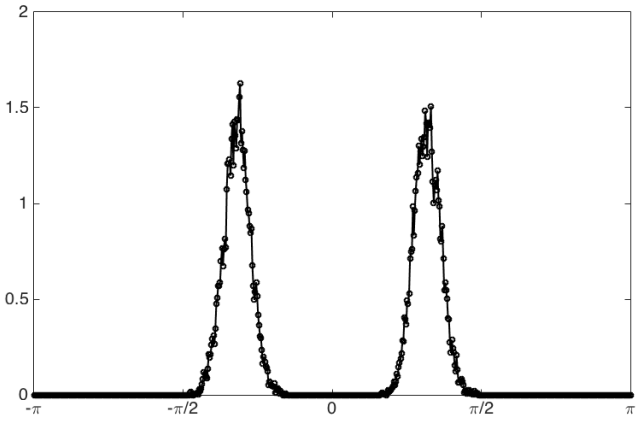

Figure 3.5: The Initial Distribution of the Velocity Directions for Two Swarms Moving into the Direction $\theta_0 = 1$ and $\theta_0 = -1$.

We vary the initial angle θ_0 and the noise level d and study the eventual long term behavior of the swarm. Two distinguished solutions are found. Their dependence on θ_0 and d is displayed in the bifurcation diagram in figure 3.6. For small θ_0 an equilibrium solution is found where the particles remain evenly dispersed in space and all have a common up-

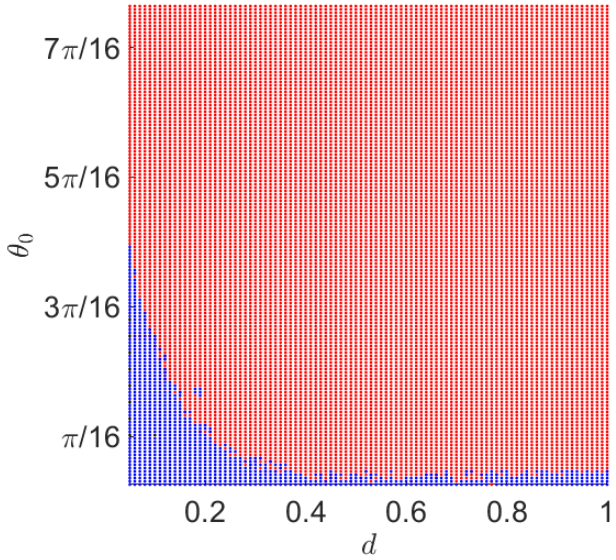

Figure 3.6: Bifurcation Diagram Displaying the Transition from Homogeneous Solution to Shear Flow. The parameters θ_0 and d for the initial velocity distributions and noise levels are illustrated in figure 3.5. We simulate each considered point in the plot 50 times. If 45 or more simulations exhibit a shear flow solution, we mark the point red. Otherwise, the point is marked blue. The channel width is $L = 10$. N, ϵ, R, and Δt are set to default. The simulations run for 100 time units.

ward or downward motion. We call this equilibrium state the homogeneous solution. The homogeneous solution is the swarming solution discussed in Section 3.2.

As θ_0 increases a time dependent solution appears, where the particle flow oscillates between a high density flow upwards at the left boundary and a high density flow downwards at the right boundary. This time dependent state is named the *shear flow solution*.

To understand its dynamical origin, we write the velocity of the particle with label j as

$$\tilde{\omega}_j = [-(v_x)_j, (v_y)_j]$$

where $(v_x)_j$ is the x-component and $(v_y)_j$ is the y-component velocity of the particle moving towards the boundary at $x = 0$. Since the normalization velocity constraint remains active for reflecting particles, on average $v_x \approx 0$ at the wall, leaving $|v_y| \approx 1$.

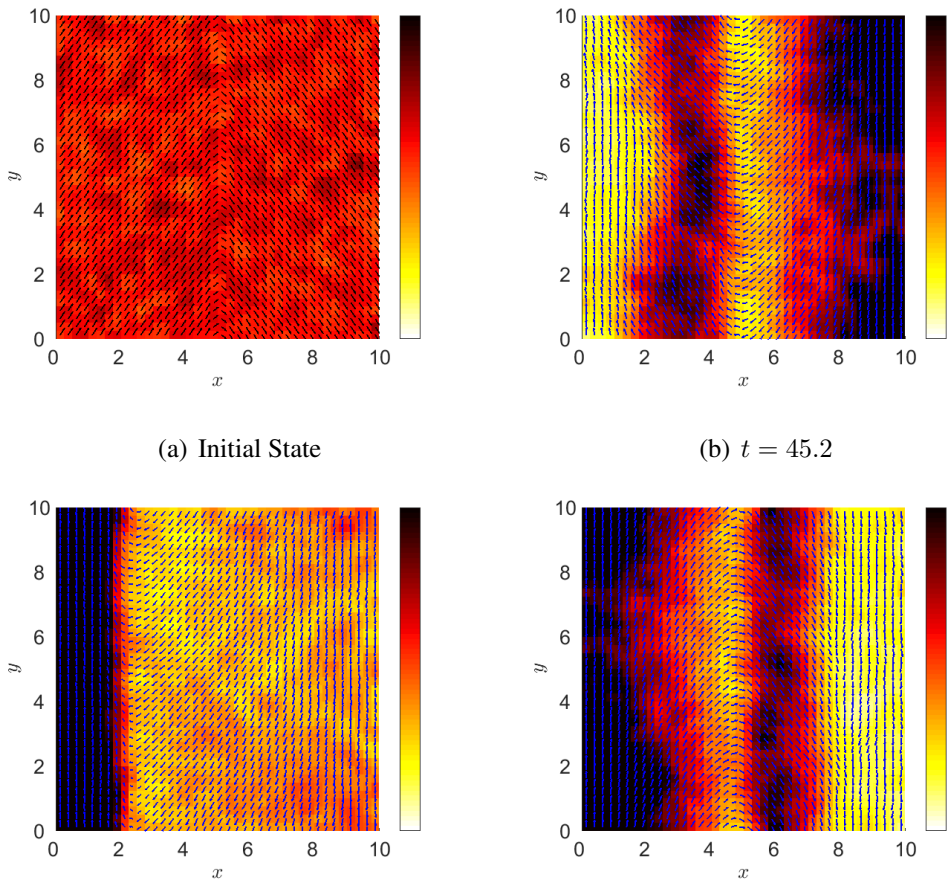

(a) Initial State

(b) $t = 45.2$

(c) $t = 46.1$

(d) $t = 47.3$

Figure 3.7: Time Progression of the Particle Density and Velocity Plots for the Shear Flow Solution. The average density in each cell is represented by a color code where yellow implies low density and black implies high density. The average velocity is represented by an arrow in the center of the cell. a) Initial state, b) at time $t = 45.2$, c) at $t = 46.1$ and d) at $t = 47.3$. The channel width is $L = 10$, noise level $d = 0.2$ and initial angle $\theta_0 = 1$. N, ϵ, R, and Δt are set to default.

The initial state of our Riemann Problem (figure 3.5) has a collective upward motion on the left and the collective downward motion of on the right. If these motions are preserved, we have a shear flow illustrated for different times in figure 3.7.

To study the dependency on parameters of the shear flow solution we compute the period of the oscillation, i.e. the time it takes for the traveling wave to return to its starting position.

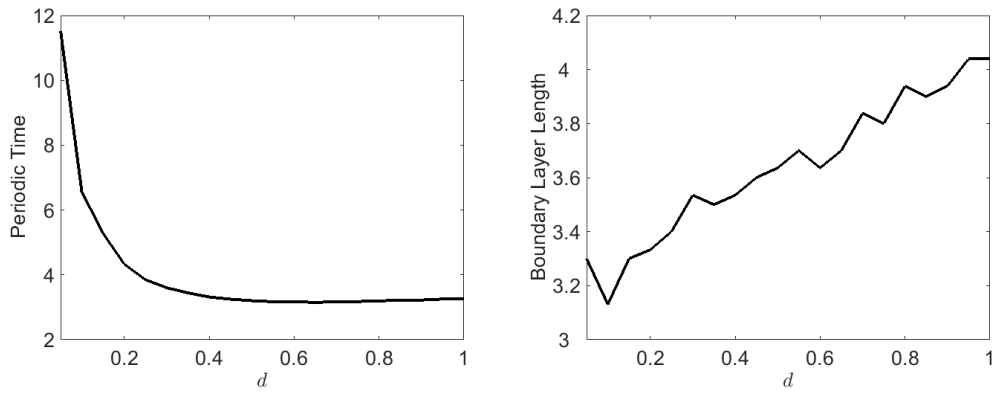

(a) Period (b) Thickness

Figure 3.8: Periodic Time and Boundary Layer Thickness for Various Noise Levels d. We compute the periods a) and boundary layers b) from 400 time units to 500 time units and from 900 time units to 1000 time units. We average these values and plot the results. Simulation parameters are set to figure 3.7 but d varies.

Figure 3.8a shows that as d increases, the period decreases. This is somewhat counter-intuitive since at higher noise level, the average of the von Mises distribution goes to zero and hence one would expect the period to increase.

To understand the details of the shear flow we study the interaction of an arriving swarm with the left boundary in several steps:

1. Assume a particle population at the left boundary that has a velocity $v = (0, 1)$. As a result the transverse velocity is zero and the particles are not leaving the boundary. Consider a swarm that is approaching the left boundary, i.e. all particles have a negative velocity in the x direction. Particles close enough to the wall will have a positive velocity in the y-direction. Assume that particles further away from the wall will have a negative v_y and define $x = M$ to be the position of the zero v_y velocity. Since the whole swarm is moving left, so is the front position M.

2. Given that the velocity has norm 1, it is easy to see that the velocity function $v_x(x)$ has a local minimum at $x = M$ and is zero at the left boundary (in fact, depending on the noise level, it may be slightly positive). The minimum in v_x leads to a compression

of particles in front of M and a dilution of particles behind M. Particles that moved through M from right to left will go from a mean velocity that has $v_y < 0$ to a mean velocity that has $v_y > 0$. and thus increase the mean v_y and hence slow down the movement of the swarm, including the movement of M.

3. As a result the boundary layer at the left boundary at which $v_x \approx 0$ grows until $v_x(M) = 0$. At that position and at that moment, the mean velocity at $x = M$ is zero and the eventual mean velocity will be determined by the noise. At that moment a small perturbation with $v_x(M) > 0$ will lead to an amplification and a wave that generates a movement of a swarm to the right. In this case the x-velocity at the front M will become a maximum, leading to a density depression trailing the wave ensuring that eventually a significant number of particles will be stuck at the left wall and will not participate in the swarm movement to the right.

We compute the thickness of the boundary layer based on the average velocity of particles $\bar{v} = (\bar{v}_x, \bar{v}_y)$. When all particles collect at the left wall (see figure 3.7), $\overline{v}_y$ approaches a maximum since all particles within this region will have an upward motion. When the particles begin to drift right, $\overline{v}_y$ decreases and particles leave the wall. Hence the *time* when the wave leaves the wall is given when $\overline{v}_y$ is maximal. At that time $\overline{v}_y$ has a velocity profile in x, starting from large positive values near the wall and going to negative values as x increases. The point where the profile goes through zero defines the thickness of the boundary layer. At this distance from the left wall, the particles are starting to drift away and move to the right. Figure 3.8b shows that the boundary layer thickness increases linearly with the noise level. Hence the wave traveling back and forth has to cover a shorter interval for larger noise and hence the period decreases as the noise increases.

The process depends on the fact that particles close to the wall have a one-sided average, ie. a high density at the wall in a boundary layer is balanced with a low density over a

much larger region in the middle of the channel. Hence, as R increases, the boundary layer increases (figure 3.9b). However, in contrast to varying d (figure 3.8a) the period increases with R (figure 3.9a). Essentially, as R increases the velocity average is taken over more and more particles, generating inertia to change and thus lengthening the period of an oscillation. Thus the scaling behavior of the period with respect to noise is anti-correlated with the scaling behavior with respect to R: reducing R is equivalent to increasing noise and vice versa.

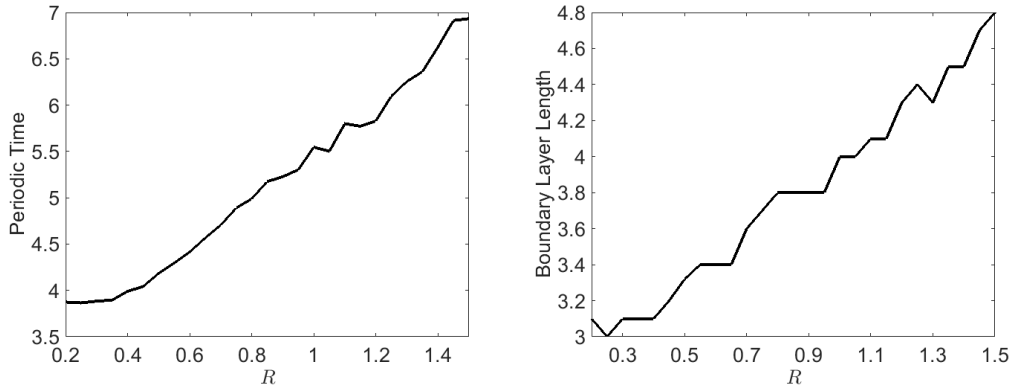

(a) Period (b) Thickness

Figure 3.9: [Periodic Time and Boundary Layer Thickness for Various Vision Horizons R. We compute the periods a) and boundary layers b) from 400 time units to 500 time units and from 900 time units to 1000 time units. We average these values and plot the results. Simulation parameters are set to figure 3.7 but R varies.

This anti-correlation suggests that if R is small enough and d large enough, the instability will remove enough particles from the wall, such that they do not have enough influence any more to maintain the initially prescribed flow at the boundary, leading eventually to the homogeneous flow solution. Indeed, for $R = 0.1, d > 0.5$ the ratio of homogenous to shear flow solutions for the initial direction angle $\theta_0 = 1$ increases relative to the ratio for $R = 0.5, d > 0.5$ confirming the suggestion.

3.5 Circular Domain

We consider swarming behavior in a disk with radius R_D. Initially, all particles are uniformly distributed within the disk and the initial velocity is uniformly distributed on the unit circle.

In the paper by Motsch and Navoret (2011) a steady states for the macroscopic Vicsek Model in to polar coordinates of the form

$$\begin{aligned} \rho(r) &= Ar^{c_2/d} \\ \Omega(\theta) &= [-\sin\theta, \cos\theta] \end{aligned} \tag{3.5}$$

has been found and called the *mill solution*. Here r is the radius from the center of the domain, A is an arbitrary constant and c_2 is a constant depending on the model parameters. The derivation of the steady state considers no boundary conditions. Solutions of this form (3.5) rotate about the center of the domain with unit speed while the density profile grows without bound.

As the mill solution has no flux through a concentric circle it may be adapted to a finite circular disk with no-flux boundary conditions, i.e

$$n \cdot \Omega = \cos\theta(-\sin\theta) + \sin\theta\cos\theta = 0,$$

where n is the normal vector to the circle.

The constant A can be explicitly found in this case by noticing that the total mass of the system remains constant. For the macroscopic model radius $R_D^\epsilon = \epsilon R_D$ of our circular domain and for an initial density ρ_0, A is found by solving the equation

$$2\pi(R_D^\epsilon)^2\rho_0 := 1 = \int_0^{2\pi}\int_0^{R_D^\epsilon} Ar^{c_2/d} r dr d\theta \tag{3.6}$$

giving

$$A = \frac{(c_2/d+2)}{2\pi}(R_D^\epsilon)^{-c_2/d-2}. \tag{3.7}$$

To compare the long-term particle behavior of the microscopic model to the mill solution of the macroscopic model (3.5) we compute the total mass fraction inside a concentric circle with radius $\bar{r}$.

$$\begin{aligned} M(\overline{r}) &= \int_0^{2\pi} \int_0^{\overline{r}} A r^{c_2/d} r dr d\theta \\ &= \left(\frac{\overline{r}}{R_D^\epsilon} \right)^{c_2/d+2} \end{aligned} \tag{3.8}$$

In addition, for every noise level d we calculate the radius of the circle that contains half of the total mass by solving $M(\overline{r}_{0.5}) = 1/2$ giving

$$\overline{r}_{0.5} = 2^{\frac{-1}{c/\lambda+2}} R_D^\epsilon. \tag{3.9}$$

Similarly, we calculate the density profile of the microscopic simulations and compute the total mass of the particle system $M_{N(\overline{r})}(\overline{r})$ where $N(\overline{r})$ is the total number of particles within the radius $\overline{r}$, $\overline{r} \leq R_D$. Scaling the system so that the total mass is one at $\overline{r} = R_D$, we find

$$M_{N(\overline{r})}(\overline{r}) = \frac{N(\overline{r})}{N} \tag{3.10}$$

Comparing $M(\overline{r})$ and $M_{N(\overline{r})}(\overline{r})$ for several noise values d, we see that the two curves match nicely (see figure 3.10). As d decreases, $M(\overline{r})$ approaches a delta function suggesting that all particles are found distributed on the boundary. For larger d, $M(\overline{r})$ scales with $\bar{r}^2$ indicating that particles are uniformly distributed within the circle.

For the microscopic simulations in the disk we determine the radii where $M_{N(\overline{r})}(\overline{r}) = 0.5$ and compare them to the $\bar{r}_{0.5}$ in figure 3.11. The curves match well. Since at higher noise d the particles are uniformly distributed within the circle, the two curves approach a lower bound given by $\bar{r} = \frac{R^D}{\sqrt{2}} \approx 3.53$ for $R^D = 5$.

Figure 3.11 indicates that the mill solution is attracting. Linear stability of the mill is provided by Degond and Yu (2015). The close match between the macroscopic mill solution and the microscopic particle simulation is unexpected: While the mill solution (3.5) has a density distribution that rotationally invariant, the actual swarm moves as a

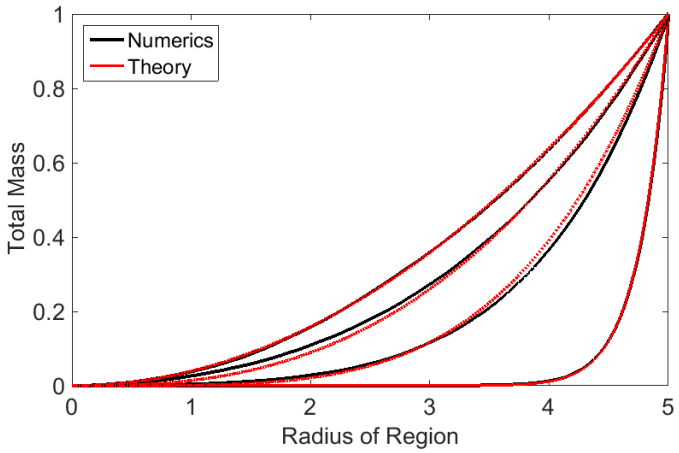

Figure 3.10: Total Mass Profile in the Disk for Several Noise Values d. The curves from left to right correspond to a decreasing d. We plot $M(\overline{r})$ (Eq. 3.8) (red) and $M_{N(\overline{r})}(\overline{r})$ (Eq. 3.10) (black) for each of the considered d values. Number of particles $N = 10000$, circle radius $R_D = 5$, and $d = 5,\ 0.5,\ 0.25$, and 0.05. ϵ, R and Δt are set to default. The simulations run for 500 time units with the plotted values being averaged over 30 simulations.

localized blob around the circle as can be seen in Fig. 3.12a). The corresponding trajectory of its center of mass is a concentric circle, Fig. 3.12b). Averaging the motion of the blob over time, we obtain the density profile of the mill solution, Fig. 3.12c). This equivalence suggests that for stationary flows the time average of the particle simulation become the equilibrium solutions in the long time scaling that is the base of the macroscopic model.

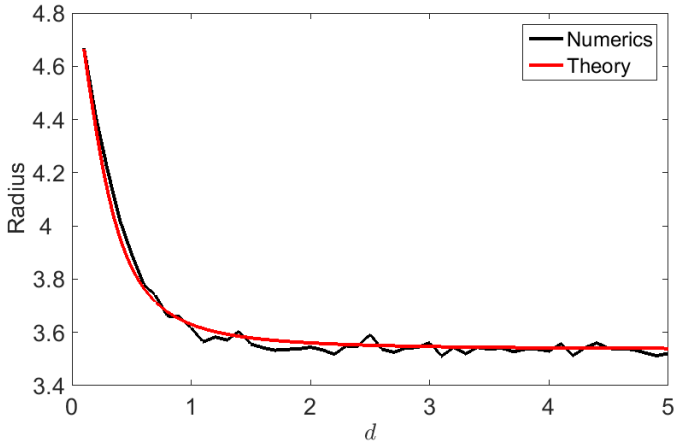

Figure 3.11: Location for Half of the Total Mass for Varying Noise Values d. We plot equation $\bar{r}_{0.5}$ (red) and the corresponding radii for half of the total mass of the particle simulations (black). Same simulation details as in figure 3.10.

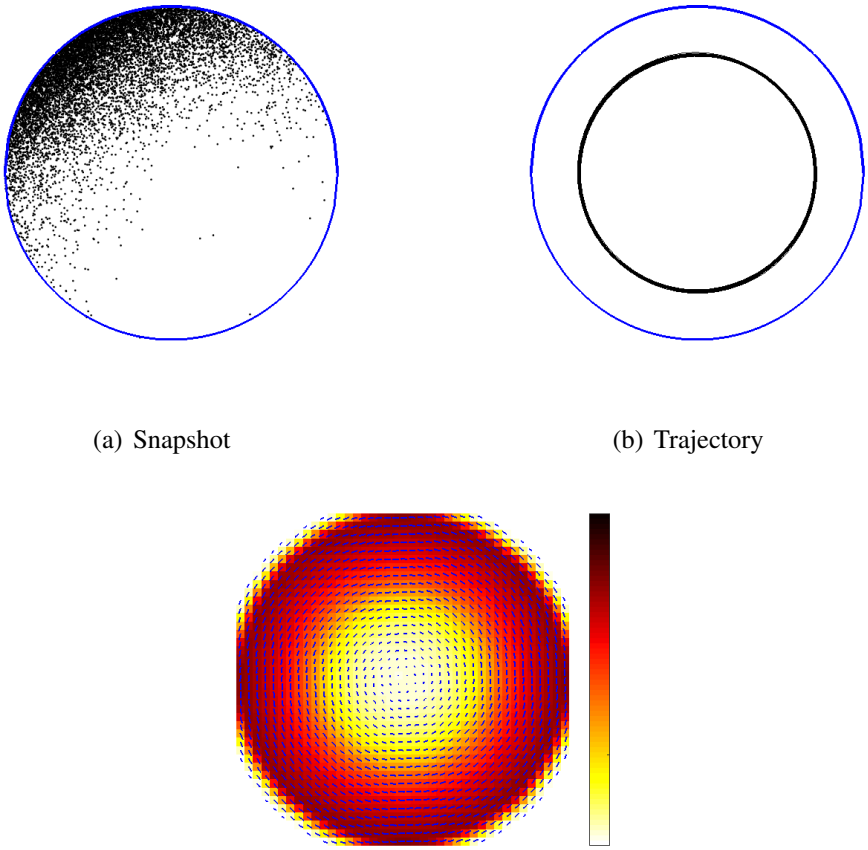

(a) Snapshot

(b) Trajectory

(c) Density

Figure 3.12: A Rotating Swarm in a Disk. a) A snapshot, b) trajectory of the center of mass. c) time average of the density. Circle radius $R_D = 5$, $d = 0.1$, and all other parameters set to default. The simulations run for 1000 time units. Rotation is clockwise.

3.6 Square Domain

We study the long term behavior of the Vicsek Model in a square box of size L. All particles are initially uniformly distributed within the box with initial velocities uniformly distributed on the unit circle. Similar to our analyses of swarms in the disk, we measure the total mass profile as

$$M_{N(l)}(l) = \frac{N(l)}{N}, \tag{3.11}$$

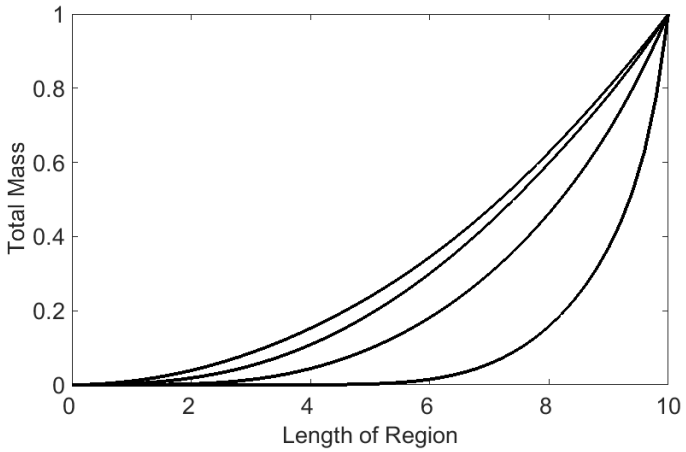

Figure 3.13: Total Mass Profile in the Square for Several Noise Values d. The curves from left to right correspond to a decreasing d. We plot Eq. (3.11) for rotating swarms in a square box. Number of particles $N = 10000$, box size $L = 10$, and $d = 5, 0.5, 0.25$, and 0.05. ϵ, R and Δt are set to default. The simulations run for 500 time units with the plotted values being averaged over 30 simulations.

where $N(l)$ is the total number of particles within a square of length $l, l \leq L$, centered on the domain and N is the total number of particles.

The density profiles (figure 3.13) show that particles are more highly concentrated near the boundary for smaller noise level d and become more evenly dispersed as d increases. Following the analysis for the disk we show that the trajectory of the center of mass trajectory for these selected d values (figure 3.14) is periodic with very little noise dispersion. The corresponding particle motion is a localized swarm that rotates about the center of the domain.

As usual, when d is large enough, the swarm loses coherence and the particles perform a random walk in the square, leading to a uniform density distribution. However, when the noise d is small enough but not equal to zero, the swarm also loses predictability and its center of mass follows a seemingly chaotic trajectory (figure 3.15b).

The reason a deterministic swarm shows a irregular trajectory can best be understood by a thought experiment: Assume a spatially extended swarm moves towards a horizontal boundary with uniform velocity normal to the boundary. When the leading edge of the

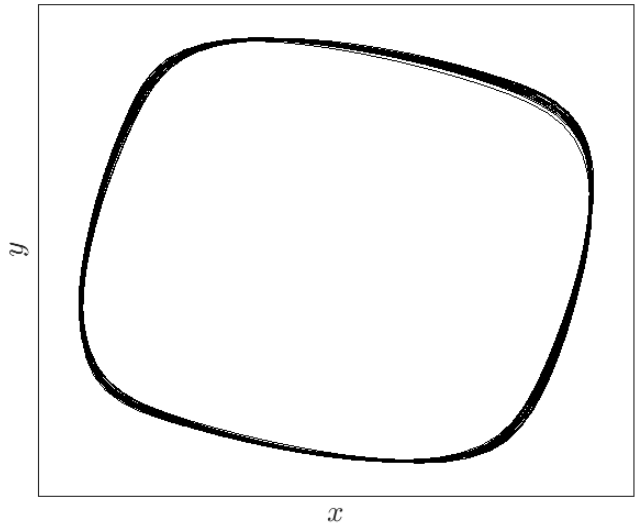

Figure 3.14: Limit Cycle Trajectory for the Center of Mass of a Swarm in a Square. Parameters are set to figure 3.13 for $d = 0.06$. The simulations run for 1000 time unit. The figure shows the last 50 time units. Rotation is clockwise.

swarm hits the boundary, most of the swam is still moving towards the boundary. Hence, the average velocity of the swarm is still towards the boundary and the leading particles get stuck at the boundary. The time when the swarm rebounds and leaves the boundary is determined by the ratio of the number of particles that hit the boundary within one time interval of the discrete update and the number of particles that do not hit the boundary in that time interval. If that ratio is above 1, then the swarm leaves the boundary.

When the ratio is approximately one, the average velocity that determines the next direction of movement is almost zero and very susceptible to slight perturbations. Any small perturbations will be greatly amplified since the velocity is normalized and the small velocity vector is divided by a normalization constant that is almost zero. As a consequence, the motion of the swarm after its collision is hard to predict.

In figure 3.15a), we include the average velocity of the particles ϕ_N as a function of time. When the average velocity is small $\phi_N < 0.35$, we see the chaotic situation where

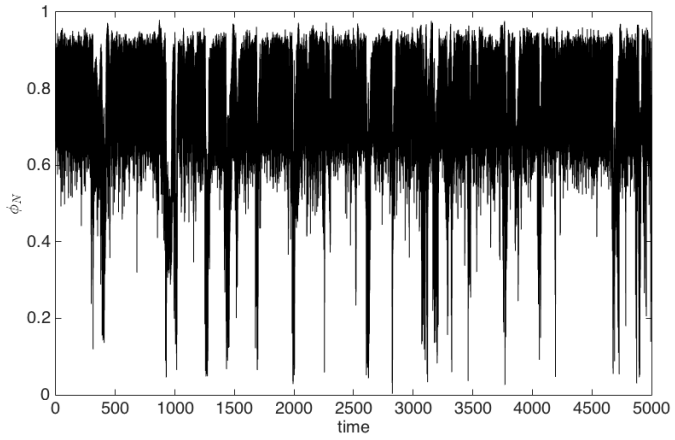

(a) Average Velocity ϕ_N

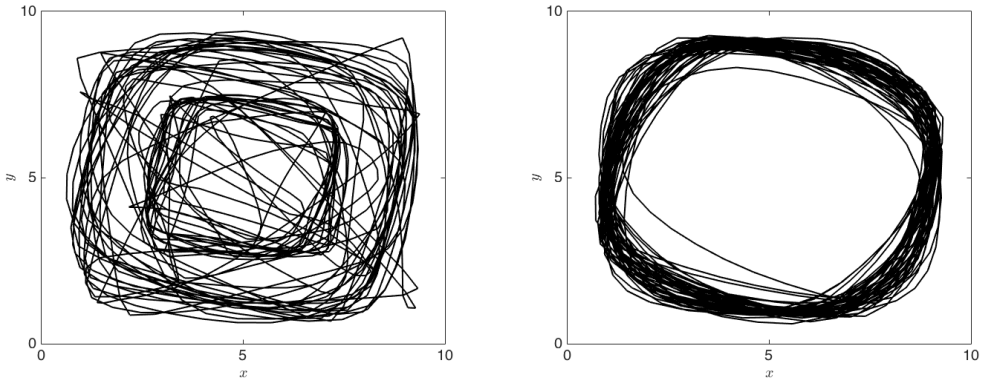

(b) Chaotic Center Of Mass: $t = 900$ to 1050 (c) Limit Cycle Center Of Mass: $t = 500$ to 650

Figure 3.15: Chaotic Trajectory for the Center of Mass Trajectory of a Swarm in a Square. a) Average velocity. b) Average velocity $\phi_N < 0.35$. c) Average velocity $\phi_N > 0.45$. We initialize with the rotational state seen in figure 3.14 with the same parameters and decrease the noise level $d = 0.035$. The simulation runs for 5000 time units.

the particle Center of Mass follows no clear path (b). However, when $\phi_N > 0.5$ in (c), we see a rotational path that is not as clearly defined as 3.14.

When the particle mass approaches the boundary, the particle velocities average out to zero, giving the gaussian noise the ability to overpower the contribution from the average velocity. When the velocity is normalized, the swarm has a random direction and fails to align with the boundary.

3.7 Discussion

We numerically analyzed the Vicsek Model in bounded domains and showed that the major effect of the boundaries was their *stickiness* which led to spatial coherence of swarms. The lack of spatial coherence in the Vicsek Model was previously considered a major flaw of the model and additional attractive forces had been postulated to remedy this flaw. Our simulations suggest, that at least in finite domains of reasonable size, the boundaries might act as the attractors and hence no further forces were needed.

Specifically, we studied three domains, 1-d channels, squares and disks. We assumed specular reflection for the individual particle and showed that the swarm as a whole interacts in-elastically with the boundaries.

- In the channel with periodic boundary conditions along the channel direction, we found the swarming solution previously described for periodic domains by Motsch and Navoret (2011) and matched their velocity to the theoretically derived von Mises distribution, Degond and Motsch (2008a). In addition, we found a new type of solution for the Vicsek Model corresponding to a periodic solution similar to a shear flow. The particles moved in opposite directions along the channel walls and the majority of the particles traveled from one boundary to the other and back, changing their flow direction parallel to the wall.

- A swarm progressing in a disk had spatial coherence and slipped along the boundary of the disk. The coherence increased as the noise level decreased, asymptotically leading to a δ-density distribution. The most notable feature of this periodic solution was that its time averaged density was numerically identical to the density of a mill solution of the macroscopic Vicsek Model, restricted to the disk. This suggested the open problem to prove under what conditions the time average of a particle model simulation became the equilibrium solution of a macroscopic model that was derived for large time and spatial scales.

- Simulations in square domains led to solutions that were structurally similar to those occurring in the disk: Coherent swarms broke the D^4 symmetry of the square and started to rotate. The center of mass described a closed trajectory that was rotationally symmetric but not reflection symmetric (C^4-symmetry). When the noise was too large, the rotational pattern was lost and particles were seen evenly dispersed in the domain. The time averaged density profile showed the particles more concentrated at the boundary for small noise. When noise was extremely small, swarms were polarized when they moved between boundaries but lost this polarization when the swarm hit a boundary. As a result, the trajectory of the center of mass appeared chaotic.

Chapter 4

ELASTIC AND INELASTIC COLLISIONS OF THE ATTRACTION-REPULSION MODEL

In this chapter, we show that the flocks satisfying Definition 1 confined within a bounded domain with spectrally reflecting boundaries collide inelastically with a slight alignment to the wall. We analyze how a flock evolves within these domains by varying the interaction potential strength λ and varying the initial heading θ_0.

We extend these observations to scattering experiments where to flocks are set to collide.

4.1 Simulation Setup

We use a 4th order Runge-Kutta method to compute the numerical approximation to system (2.9). For all potential pre-factor λ values, the eigenvalues of the system lie within the stability region for a time step of $\Delta t = 0.1$. We note that very long simulation runs produce reproducible results, indicating that even with the addition of reflecting walls, the algorithm is still stable.

When reaching the reflecting boundary, a single particle will experience specular reflection and its velocity is updated

$$v_{new} = v_{old} - 2(v_{old} \cdot \vec{n})\vec{n} \tag{4.1}$$

where $\vec{n}$ is the normal vector to the boundary. A particle j interacting with the wall at time step $n\Delta t$ will not update its velocity according to Eq. (2.9) until the next time step $(n+1)\Delta t$. That is, we have a time step $(n+\zeta)\Delta t$ with $0 < \zeta < 1$ that is between $n\Delta t$ and $(n+1)\Delta t$ where the velocity $v_j^{n+\zeta_j}$ is updated according to Eq. (4.1) and continues on this

reflected path until $(n+1)\Delta t$. At the time step $(n+1)\Delta t$ the velocity updates according to Eq. (2.9). When set in a reflecting domain, the Attraction-Repulsion Model experiences the same discontinuity as explained in the Vicsek Model in Chapter 3. We keep $\Delta t = 0.1$ to avoid conflicting results that depend on the time step choice.

Other choices for the exact numerical reflection algorithm are possible. For instance, the authors in D'Orsogna *et al.* (2006) implement a multistep method Adams-Bashforth-Moulton. We discuss our choice for numerical method in Appendix B.

For all simulations, we initialize the system with a flock satisfying Definition 1 where m_0 is dependent on the initial heading $\theta_0 \in [0, 2\pi)$ and the angle θ_0 is calculated from the positive x-axis

$$m_0(\theta_0) = \sqrt{\alpha/\beta}[\cos(\theta_0), \sin(\theta_0)] \tag{4.2}$$

The parameter choices for each simulation (unless stated otherwise) are: ratio between strength of repulsion and attraction $C = 10/9$, ratio between the length of repulsion and attraction $l = 3/4$, number of particles $N = 100$, friction force $\beta = 5$, acceleration force $\alpha = 1$, potential pre-factor $\lambda = 25$, initial heading $\theta_0 = 0$, and $\Delta t = 0.1$. We average all findings over 10 spatial rotations and run most simulations for 500 time units to 10000 time units. We run the same experiments with $N = 200$ and find similar results.

Simulations were run using MATLAB on 96gb RAM and 2 Intel(R) Xeon(R) CPU E5-2620 0 @ 2.00GHz processors and the average time for 5000 time units took 1200 seconds.

4.2 Scattering a Single Swarm at Boundaries

We will try to understand multiple swarm collisions within a bounded domain as a sequence of single wall collisions.

4.2.1 Single Wall Collision

Individual Particle Motion

We consider the Attraction-Repulsion Model (2.9) in an unbounded half-space in R^2 with a specularly reflecting wall at $x = L$. We initialize a flock to collide with the wall with initial headings $\theta_0 \in [0, \pi/2)$. When $\theta_0 = \pi/2$, the flock translates upward, i.e. is parallel to the wall and hence never interacts with the wall. We note that in free space, a flock will remain intact and continue on its set trajectory for all time.

There are two limiting cases for the interaction of the swarm with the wall: For small λ all particles directly hit the wall and bounce back specularly. This is illustrated in figure 4.1a) and c). For large λ only about the leading 2/3 of the particles physically hit the wall and bounce back. The other particles experience a changed interaction potential due to the change in velocity and position of the leading particles. The changed potential creates a differential slowing down within the swarm, leading the trailing particles to turn around before they hit the wall. This is illustrated in figure 4.1b) : the maroon colored left part of the swarm will not hit the wall but turn around earlier. The resulting reflected swarm experiences strong internal mixing. Figure 4.1d) shows that the initially leading particles and the initially trailing particles mix homogeneously.

Figure 4.2 shows the numbers ratio of those particles that hit the wall, to all particles within the flock as a function of starting angles θ_0 and potential pre-factors λ. We see that the ratio decreases with increasing λ and increasing initial angle. To characterize the internal remixing of the swarm after it hits the wall for an incoming direction $\theta_0 = 0$, we determine the initial position in the swarm along the x-axis that separates particles that directly hit the wall and those that do not (see Fig. 4.1b). Figure 4.3 shows a sharp bifurcation: for $\lambda < 13$ the position that separates the two behaviors is at the trailing edge

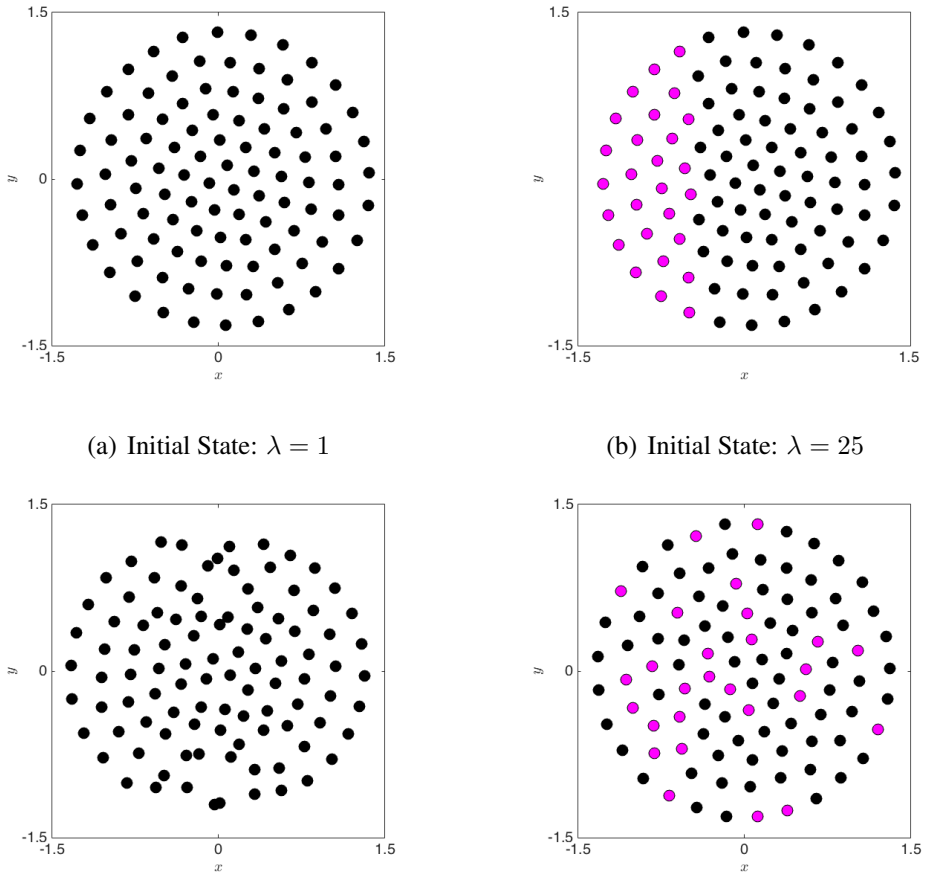

(a) Initial State: $\lambda = 1$

(b) Initial State: $\lambda = 25$

(c) End State: $\lambda = 1$

(d) End State: $\lambda = 25$

Figure 4.1: A Swarm Impacting a Vertical Wall with Initial Heading $\theta_0 = 0$: Initial and End State of the Swarm. Particles that directly interact with the wall are colored black and particles that do not interact with the wall are colored maroon. a) All particles hit the wall for $\lambda = 1$, b) the trailing particles turn around before they hit the wall for $\lambda = 25$. c) and d) Depicts the end state of the flock; the location and of particles after the swarm reflect.

of the swarm, i.e. all particles hit the wall, whereas for $\lambda > 13$ that point moves linearly forward.

It is instructive to determine the time it takes the flock to switch directions in this experiment. We consider the time when the last particle of the swarm turns around (i.e. v_x changes direction) as the swarm turning time and call it t_{turn}. It is represented by the black in figure 4.4a) as a function of λ. We compare swarm turning time to the time to turn around for the most distant particle from the wall (shown in red). Both values coincide and

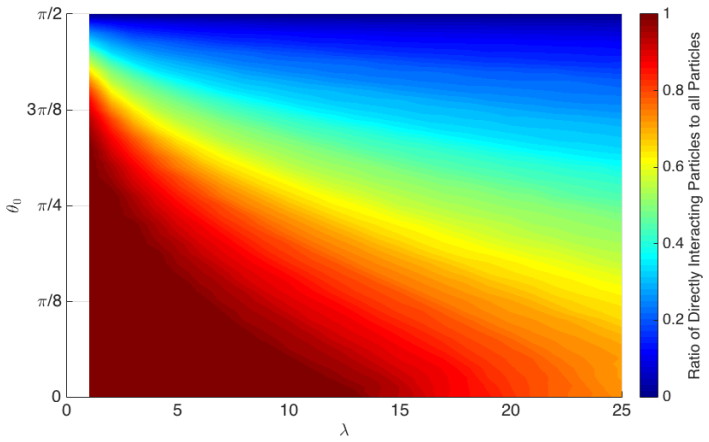

Figure 4.2: Ratio of Directly Interacting Particles to All Particles as a Function of λ and the Initial Heading θ_0.

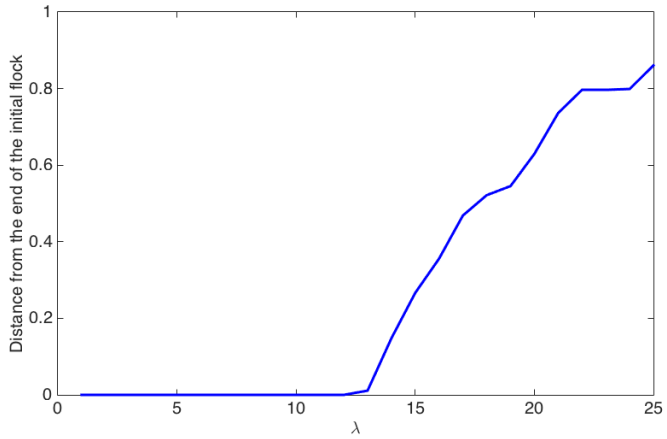

Figure 4.3: Position of the First Particle in the Direction of Motion of the Flock That Turns Around Without Hitting the Wall for $\theta_0 = 0$.

increase with λ until $\lambda = 12$. Past $\lambda \geq 14$, the swarm turning time shows a slight linear decrease while the turn times of the most distant particle show a sharp drop and then a linear decrease.

Comparing figure 4.3 and figure 4.4b) confirms that the last particle to turn is the most distant particle from the wall that actually hits the wall. Hence as λ increases past 14, the last particle to turn around moves into the interior of the swarm.

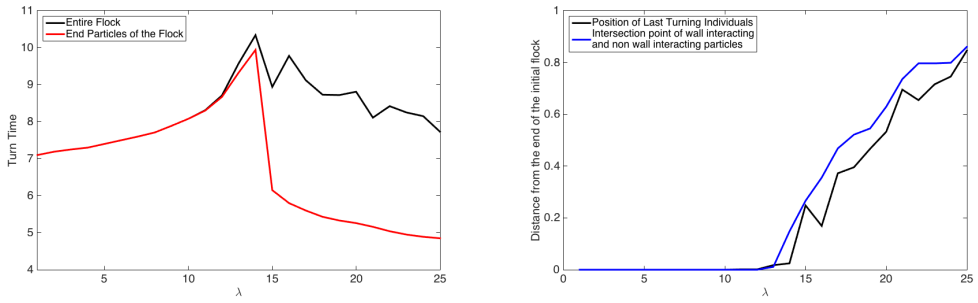

(a) Turn Time (b) x Postion

Figure 4.4: Turning Times and Turning Position for a Various λ. a) Turning time for the most distant particles (red) and for the ones that turn last (black). b) The initial position of the particle in the flock that switches direction last (black) and the position of the closest particle to the wall that does not hit the wall (blue).

Studying the kinetic energies in the x and y direction (Figure 4.5) clarifies the swarm-wall interaction: For $\lambda \approx 1$, the swarm reflection is totally specular, all the kinetic energy is in the x direction and it stays constant throughout the wall interaction.

As λ increases, the swarm slows down (decreasing total kinetic energy) and is compressed, i.e. kinetic energy is converted into potential elastic energy. As the potential energy is released, the swarm undergoes internal damped oscillations which involve the kinetic energies in the x and y direction.

As a result, the flock experiences a breathing or pulsing motion. We further examine this motion in section 4.2.3 where we perform a Proper Orthogonal Decomposition of the simulation data.

Refraction Law

We have seen that, even though individual particles follow specular reflection laws (4.1), the flock as a whole does not collide elastically but rather inelastically (see also section 4.2.3). To determine the influence of the individual paths on the reflection laws for a flock, we track the center of mass of the flock and measure the outgoing angle of its trajectory as a function of the θ_0. Figure 4.6a) illustrates the definition of the measurement of the outgoing

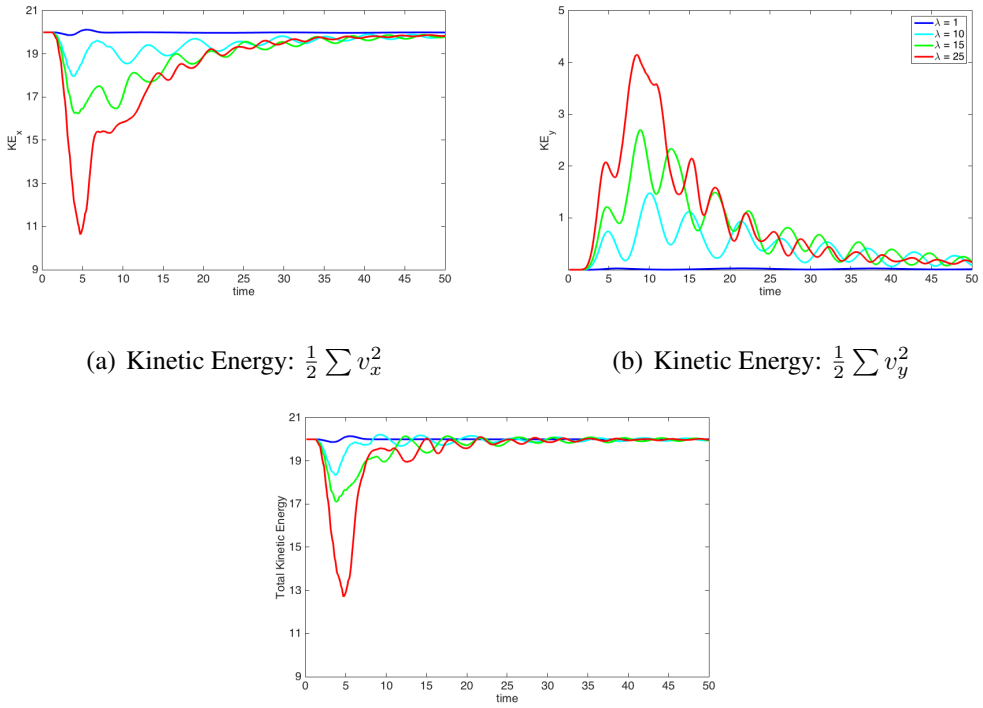

(a) Kinetic Energy: $\frac{1}{2}\sum v_x^2$

(b) Kinetic Energy: $\frac{1}{2}\sum v_y^2$

(c) Total Kinetic Energy

Figure 4.5: Kinetic Energy Transfer from the x-Direction to the y-Direction for Several λ Values.

angle. If the trajectory of the center of mass is exactly specularly reflected, by definition, θ_0 and the outgoing angle are equal. Notice that if the outgoing angle is different than the incoming, the wall interaction does not follow the reflection law but rather a refraction law.

Figure 4.6b) shows the outgoing angles as a function of the incoming angle and λ [1] We see that for increasing λ the outgoing angle aligns more to the wall than would be expected from specular reflection of the swarm as a whole. Figure 4.6c) emphasizes this result by plotting the difference between the outgoing angle and the initial angle θ_0. For small λ the flock reflects almost specularly. As λ increases, the difference the difference becomes more pronounced. In particular, when only a fraction of the particles hit the wall ($\lambda > 13$, see

[1]Note: For $\theta_0 = 0$, the flock has equal chance of reflecting upward or downward. When averaging over the spatial rotations, we take the absolute value of the outgoing angle for each rotation. Whether the flock aligns upward or downward is irrelevant at $\theta_0 = 0$.

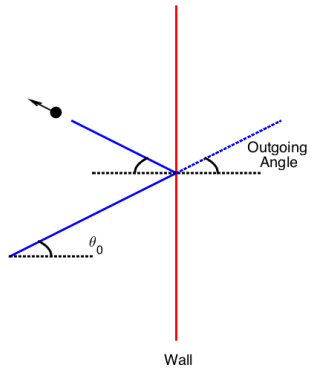

(a) Calculating Outgoing Angles

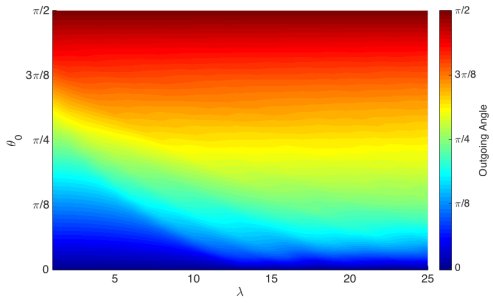

(b) Refraction Laws

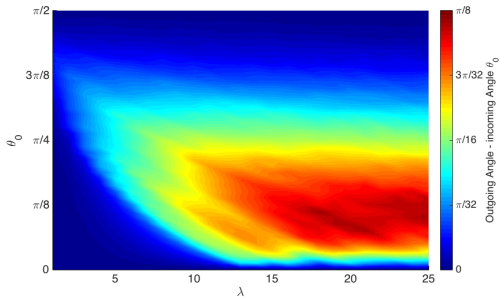

(c) Difference Between Outgoing Angles and θ_0

Figure 4.6: Refraction Law for a Flock Interacting with a Wall. a) Schematic definition of the outgoing angle. b) Outgoing angle as a function of incoming angle and λ. c) The outgoing angle minus the initial angle θ_0.

section 4.2.1), the outgoing angle differs greatly from θ_0. The flock collides inelastically leading to an alignment with the wall. Summarizing, we find two types of reflection at the wall:

1. The swarm as a whole interacts elastically with the wall, characterized by specular reflection of *all* particles leading to a specular reflection of the swarm.

2. The swarm as a whole interacts inelastically with the wall, caused by the fact that some particles do not hit the wall when they turn around. As a result, the swarm tends to align with the wall.

The behavior of the swarm bifurcates from type 1 to type 2 at about $\lambda = 13$.

4.2.2 Multiple Reflections

We can study the influence of multiple wall interactions in various geometries by considering the refraction law at a wall as a one-dimensional map, relating the incoming angle to an outgoing angle.

Hence, we can consider multiple reflections as iterated maps and study limiting behavior as the number of wall interactions goes to infinity. Convergence of the iterated map to a fixed point or to a periodic orbit corresponds to a stable periodic or period-doubled trajectory of the swarm in the geometrical domain. An unstable fixed point corresponds to an unstable periodic orbit of the swarm.

The concept of an iterated map for the swarm-wall interaction depends on the fact that the flock has fully stabilized to the free equilibrium solution before it hits the wall again.

Channel

Using Figure 4.6(b) we can construct 1-d maps of the outgoing angle as a function of the incoming angle. Figure 4.7 shows two representative maps for $\lambda = 5$ and $\lambda = 25$. In both cases, there are two equilibria: $\theta = 0$ and $\theta = \frac{\pi}{2}$, the former being unstable and the latter being stable.

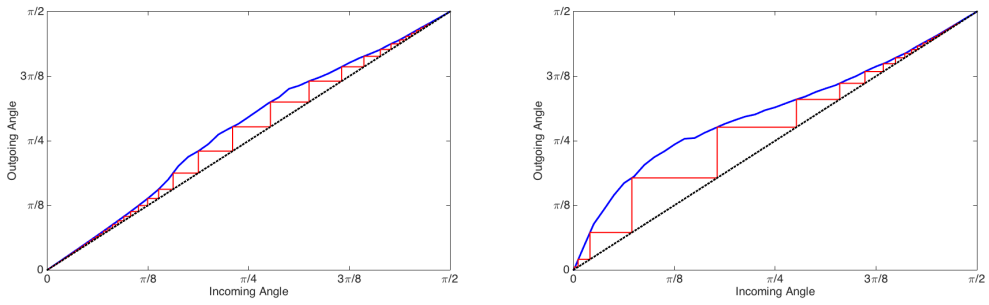

(a) $\lambda = 5$ (b) $\lambda = 25$

Figure 4.7: One-Dimensional Maps and the Staircase Diagrams for the Outgoing Angles as a Function of the Incoming Angles. a) $\lambda = 5$ and b) $\lambda = 25$.

Figure 4.8 plots the number of iterations necessary for a starting incoming angle 0 to reach an outgoing angle that is greater than 1.4.

This is a measure of the instability of the vertical reflection (θ_{e1}) and the stability of the alignment with the wall (θ_{e2}).

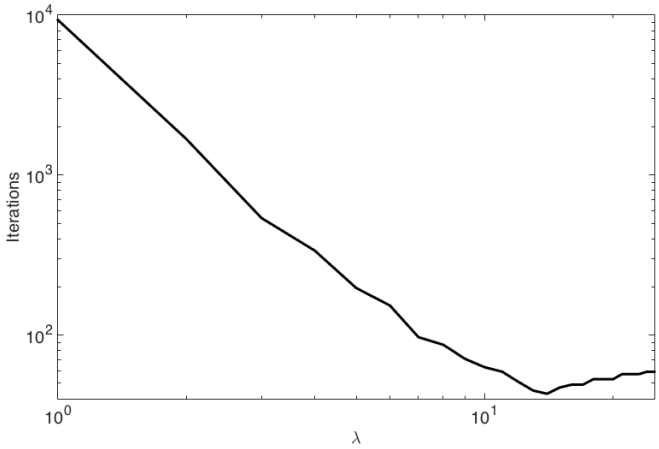

Figure 4.8: Number of Interactions with the Channel Walls Before the Flock Converges to $\pi/2$ Heading in an Open, Infinite Width Channel. The width of the channel is infinite; the flock completely stabilizes before interacting with the next wall.

To see the impact of incomplete relaxation of the swarm we reduce the channel width. For really small width the perturbations generated by the wall interactions are additive and eventually causes the flock to either break apart when the milling steady state is not stable i.e. for small λ values Chuang *et al.* (2007), or relax into the milling steady state solution for larger λ.

A representation of the transition between a narrow channel and an infinitely wide channel is achieved for a channel width of 14 units. Here, the flock has adequate time to settle but the internal oscillations have not decayed yet. We find that at most 10% of the particles break off and the remaining particle have a common heading. The milling steady state solution is never seen.

Determining a refraction law by relating the incoming and outgoing angles of the center of mass of the swarm we find the iterated maps in figure 4.9 which are qualitatively similar

to the maps in figure 4.7. The influence of the noise, generated by fast repetition of the wall interaction is seen when λ is small. For a starting angle close to zero the alignment with the wall is very weak and hence susceptible to noise. The inset in figure 4.9a) shows a case, were the swarm bounces back and forth with movements up and down before eventually settling to an alignment with the channel in the upwards direction. Noise may even trap the swarm in a horizontal back and forth motion that does not align with the channel for a long simulation time (figure 4.10).

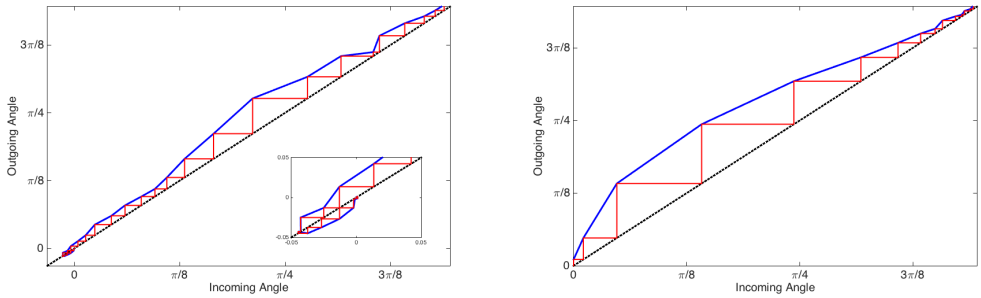

(a) $\lambda = 5$ (b) $\lambda = 25$

Figure 4.9: Swarm Trajectory for an Open Channel with Finite Width 14 Units. a) $\lambda = 5$: inset- the flock starts to drift downward but switches direction and drifts upward. b) $\lambda = 25$: the flock drifts monotonically up.

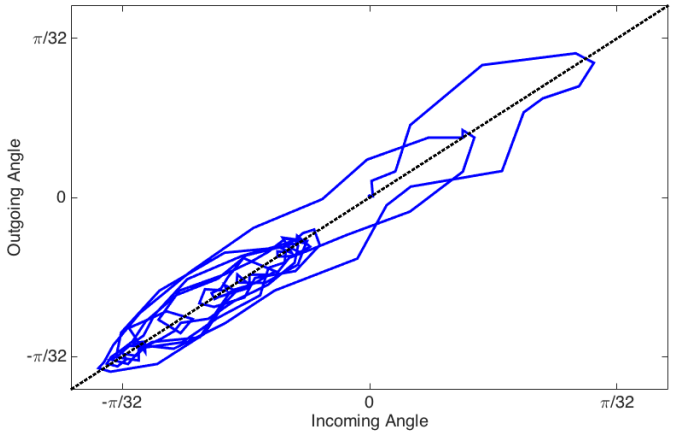

Figure 4.10: Sample Trajectory of a Swarm That is Stuck in a Horizontal Periodic Orbit for 5000 Time Units. $\lambda = 5$ with a different initial condition than in figure 4.9a).

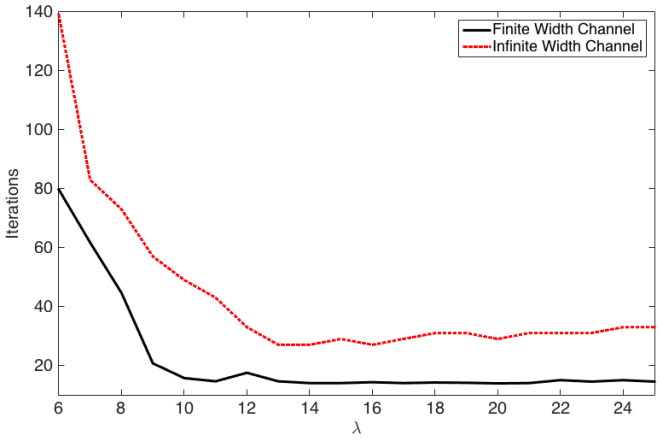

Figure 4.11: Number of Interactions with the Wall Before the Flock Aligns with the Channel for a Channel Width of 14 Units (Red) and an Infinitely Wide Channel (Black) as a Function of λ.

For $\lambda > 6$ the main effect of the wall interaction noise is to destabilize the horizontal equilibrium θ_{e1}, aligning the swarm faster with the channel direction (see figure 4.11).

Square

We characterize the trajectory of a swarm in a square by the outgoing angle $\eta \in [-\pi/2, \pi/2]$ calculated from the boundary in the direction that the swarm is moving. For clockwise rotation, $\eta < 0$ while for counterclockwise rotation $\eta > 0$. Notice that by simple geometry, the outgoing angle η_n leads to an incoming angle at the next boundary of the form $\pi/2 - \eta_n$. Thus, for specular reflection in a square the sequence of outgoing angles is $\eta_0 \to \frac{\pi}{2} - \eta_0 \to \eta_0$ for any starting angle η_0, filling the square densely with periodic orbits.

Assuming a square that is big enough and a swarm that hits a boundary far enough away from the lateral boundaries, we assume that the refraction law discussed in section 4.2.1 holds and is the same at every bounday. Hence we iterate the refraction map twice and study its fixed points and their stability to predict the swarm behavior in a square box. We then simulate actual swarms in such a box and compare the prediction with the simulation results.

Figure 4.12 shows the map, generated by two reflections, i.e. $\eta_n \rightarrow \eta_{n+2}$ for different values of λ. A fixed point of this map is a periodic trajectory of the swarm in the square domain. Figure 4.12a) shows that for small λ there are three fixed points: $\eta_{e1} = 0$, corresponding to a motion parallel to a boundary, $\eta_{e2} = \frac{\pi}{4}$ corresponding to a symmetric orbit connecting the midpoints of the sides of the square, and $\eta_{e3} = \frac{\pi}{2}$ corresponding to a motion parallel to a boundary and orthogonal to the one associated with η_{e1}. Inspection of the staircase diagrams shows that the motions parallel to the boundary are attracting while the symmetric trajectory is unstable.

Near $\lambda = 6$ (figure 4.12b)) the reflection law becomes specular, i.e. every angle results in a periodic orbit. In terms of a bifurcation we have degenerate bifurcation leading from an unstable fixed point in the interior of the interval $[0, \pi/2]$ to a stable fixed point shown Figure 4.12c) and d) via a completely linear map. As a result of the bifurcation, the motions parallel to the boundaries become unstable. The bifurcation leading to the instability of the orbits parallel to the boundaries and the stability of a rotating orbit is not instantaneous in the parameter λ. In fact there is an interval of angles containing $\pi/4$ for which the map $\eta_n \rightarrow \eta_{n+2}$ is completely linear, leading to a continuum of periodic orbits. Figure 4.13 shows the linear intervals as a function of λ. Figure 4.14 shows periodic orbits associated with the interval of angles, for which the square reflection map is linear for certain values of λ. The transition between the orbits parallel to the boundary and the rotating orbits can easily be understood in term of the refraction laws discussed in section 4.2.1. For large enough λ a swarm will reflect with the tendency to align with the wall. As a result, the orbits parallel to the wall become unstable and lead to a rotation.

Notice that, even though we analytically study an iterated map system, the actual map was generated by a simulation study of a swarm hitting a wall. Hence, the continuum of solutions indicated in figures 4.13 and 4.14 may not be all neutrally stable analytically. However, the interaction with the wall is a noisy process, depending on small variations in

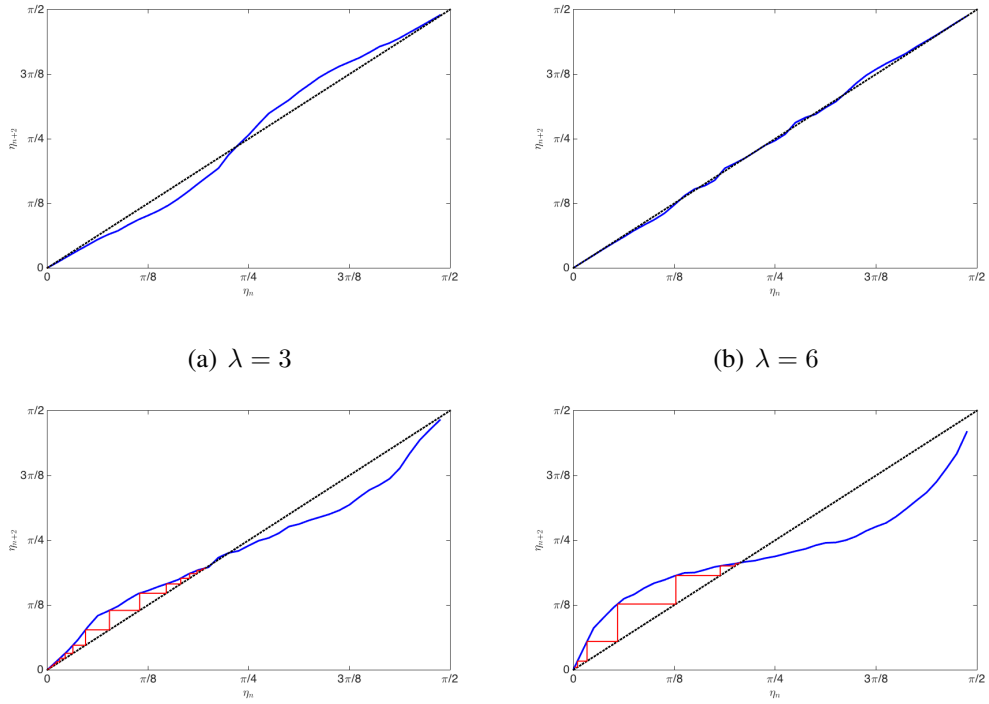

(a) $\lambda = 3$ (b) $\lambda = 6$

(c) $\lambda = 10$ (d) $\lambda = 25$

Figure 4.12: Mapping of the Reflection Angles Using the Refraction Law for Swarms in a Square Domain. We map η_n to η_{n+2} for various λ values. a) $\lambda = 3$: unstable fixed point at $\eta = \pi/4$, stable fixed points at $\eta = 0$ and $\pi/2$. b) Linear map indicates specular reflection. c) and d) $\lambda \geq 10$: the fixed points at $\eta = 0, \pi/2$ become unstable and a fixed point at $\eta < \pi/4$ becomes stable.

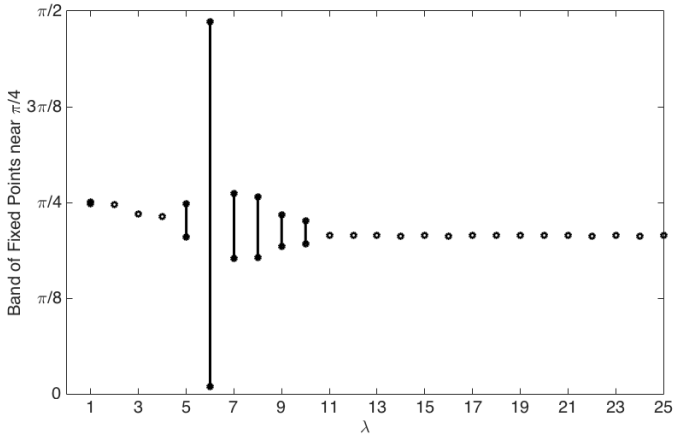

Figure 4.13: Fixed Points for the Iteration Map of the Square as a Function of λ.For $4 \leq \lambda \leq 10$, the fixed points form a continuum.

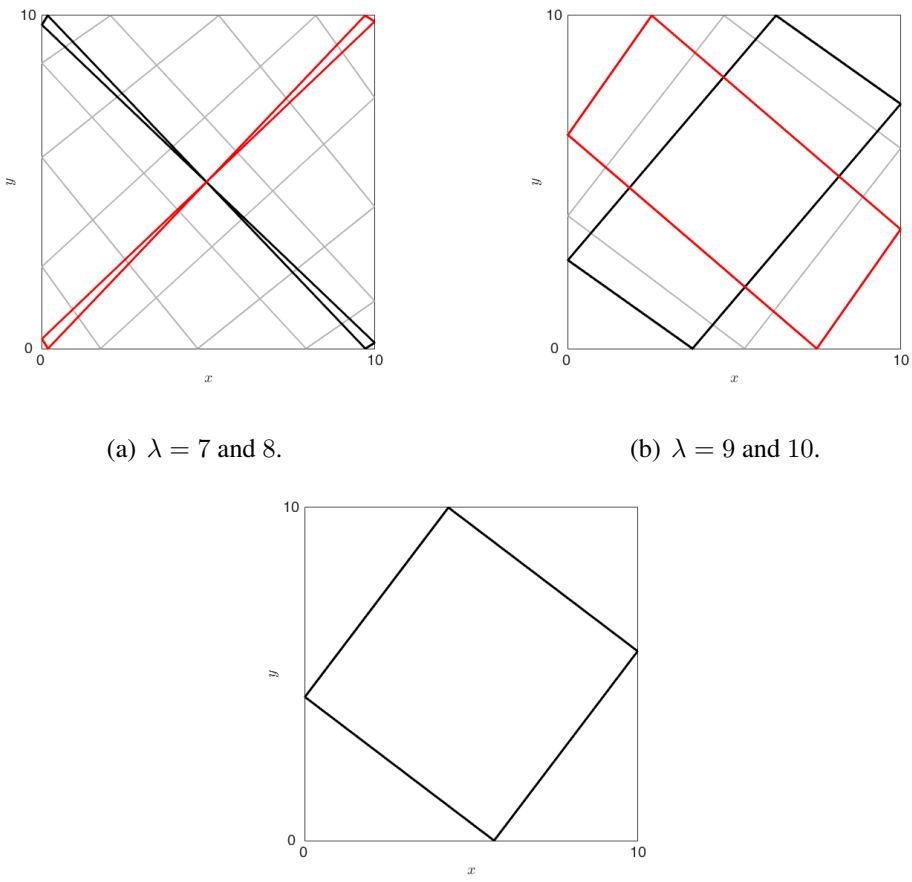

(a) $\lambda = 7$ and 8.

(b) $\lambda = 9$ and 10.

(c) $\lambda \geq 11$

Figure 4.14: Trajectory for the Minimal (Black) and Maximal (Red) Fixed Angles Seen in Figure 4.13. The grey trajectories indicate some of the trajectories in between the black and the red orbits. The bottom panel shows the one stable periodic orbit occurring for $\lambda = 11$.

the initial conditions of the swarm particles and that noise level is overwhelming any small attraction or repulsion that may be present analytically close to the bifurcation point. The situation is similar to the weakly stable transversal flow in the channel (figure 4.14).

We now numerically test our predictions based on the iterated refraction law by simulating a flock set inside a 10×10 units square. We perform two fundamental sets of experiments for different values of λ: i) we prepare an initial condition representing a flock solution of the Attraction-Repulsion Model aligned with the walls of the square and ii) we prepare an initial condition representing a rotating flock solution.

We find that the iterated map system is valid locally when the attraction or repulsion to a fixed point is strong: For $\lambda < 4$ the rotating solution is unstable while the solution parallel to the wall is stable. For $\lambda = 25$ the rotating solution is stable and looks like figure 4.14c) while the flock moving parallel to a wall is unstable. However, the attraction to these fixed points is typically not global: For small λ, If we prepare the flock in the rotating setup, it will disintegrate when it hits the corners of the square and will not reform as a swarm parallel to the walls. In the case of weakly stable fixed points for the iterated maps, $4 \leq \lambda < 7$, flocks mostly disintegrate.

Increasing $\lambda \geq 7$, we find a superposition of the neutrally stable solutions found via the iterative map. Figure 4.15a) shows the trajectory of the center of mass of a flock. It is strikingly similar to the set of neutrally stable cycles found via the iterated map analysis (figure 4.14a). Notice also that there is a frequent change in the rotation direction with on average no preference for clockwise or counterclockwise motion. As λ increases, the set of neutrally stable periodic orbits shrinks. Comparing the center of mass trajectory in figure 4.14b) with figure 4.15b) again shows good agreement between the actual trajectory and the neutrally stable set of periodic orbits. Notice though that the two figures do not correspond to exactly the same values of λ. The parameter has to be increased for the actual simulations to match the iterated map figure.

Increasing λ beyond 14, solutions cease to switch their rotation direction and move continuously from symmetry type C^2 corresponding to a trajectory that is symmetric under a rotation by π (figure 4.15c)) to a symmetry type C^4 corresponding to a rotation by $\pi/2$ (figure 4.15d)).

4.2.3 Internal Swarm Dynamics

We analyze this pulsing behavior seen in the kinetic energy that was computed in section 4.2.1. Using the Proper Orthogonal Decomposition POD, we extract a compact, rele-

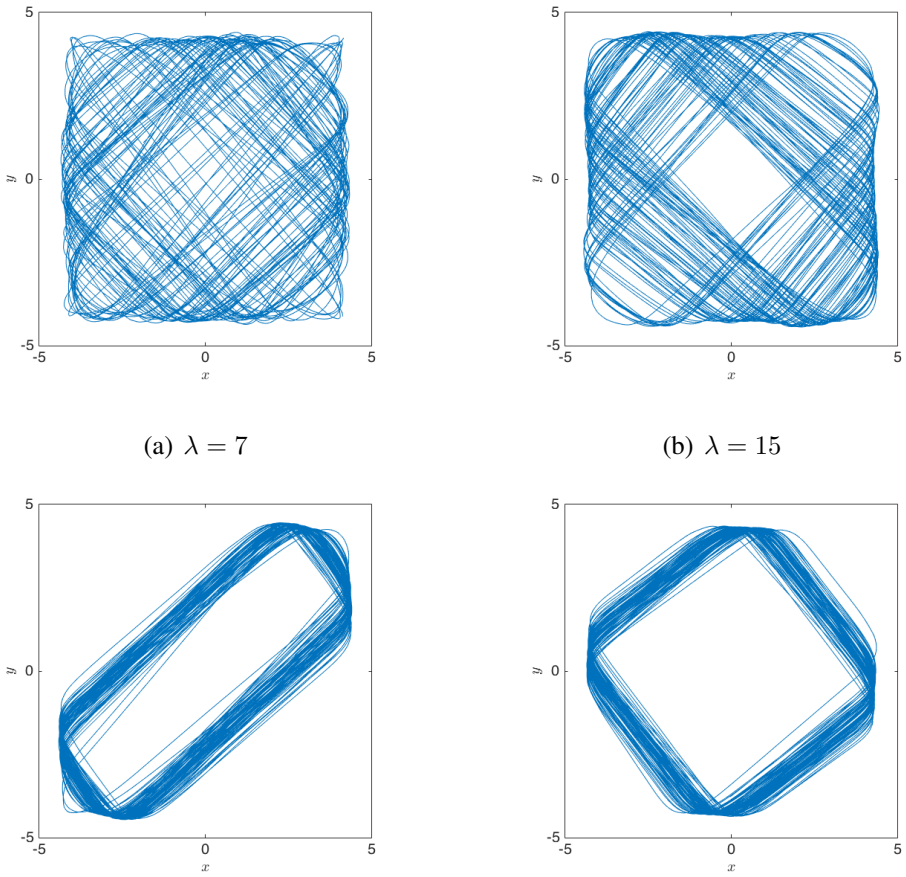

(a) $\lambda = 7$ (b) $\lambda = 15$

(c) $\lambda = 18$ (d) $\lambda = 25$

Figure 4.15: [Center of Mass Trajectory for Flocks Set in a 10×10 Box: Typical Trajectories as λ Increases. a) Trajectories rotate in both a clockwise and counterclockwise direction. b), c), and d) Trajectories only rotate in a clockwise direction.

vant representation of the numerical data. The POD, see Kirby (2000), seeks to obtain an applicable depiction of a series of snapshots $\mathbf{x}^{(k)}$ of the numerical data where $\mathbf{x}^{(k)}$ is a $4N$ column vector containing the position and velocity of each particle at time t_k:

$$\mathbf{x} = \begin{bmatrix} x_1^{(1)} & \dots & x_1^{(k)} & \dots & x_1^{(M)} \\ & \dots & & \dots & \\ x_{4N}^{(1)} & \dots & x_{4N}^{(k)} & \dots & x_{4N}^{(M)} \end{bmatrix}.$$

We subtract the center of mass from the position components and mean velocity from the velocity components so that the ensemble is centered at $\mathbf{0}$.

We seek an orthonormal basis Φ that maximizes the mean squared projection of the data onto itself. That is, we solve for the best first eigenvector $\phi^{(1)}$ as the best rank one approximation that solves the following optimization problem

$$\text{Maximize: } \langle(\phi^{(1)}, \mathbf{x})^2\rangle \qquad \text{subject to: } (\phi^{(1)}, \phi^{(1)}) = 1 \tag{4.3}$$

where $\langle\cdot\rangle$ is the average and $(\cdot)$ is the euclidean inner product. Notice that the optimization function computes the average energy for $\mathbf{x}$ along $\phi^{(1)}$ and equation (4.3) implies that this computed energy is greater than any other projection. The constraint ensures that you cannot scale $\phi(x)$ by a coefficient and increase the projection.

The optimization problem reduces to solving by Kirby (2000)

$$C\phi^{(1)} = \gamma_1\phi^{(1)} \tag{4.4}$$

where

$$C = \langle\mathbf{x}\mathbf{x}^T\rangle = \frac{1}{M}\mathbf{x}\mathbf{x}^T$$

averages the space and velocity over time and λ_1 is the Lagrange multiplier. Continuing iteratively with the requirement that $(\phi^{(i)}, \phi^{(j)}) = 0$ where $j \neq i$, the optimal basis vectors come from the eigenvector solutions of

$$C\phi^{(i)} = \gamma_i\phi^{(i)} \tag{4.5}$$

The Lagrange multipliers are ordered such that $\gamma_1 \geq \gamma_2 \geq \cdots \geq \gamma_{4N} \geq 0$, implying that $\phi^{(1)}$ gives the optimal projection.

Since ϕ forms a basis for the field $\mathbf{x}^{(k)}$, we can write

$$\mathbf{x}^{(k)} = \sum_{j=1}^{M} a_j^{(k)}\phi^{(j)} \tag{4.6}$$

where the expansion coefficients a_j are uncorrelated. Equation (4.6) written in matrix form

$$\mathbf{x} = \Phi A \qquad \text{or} \qquad A = \Phi^T\mathbf{x} \tag{4.7}$$

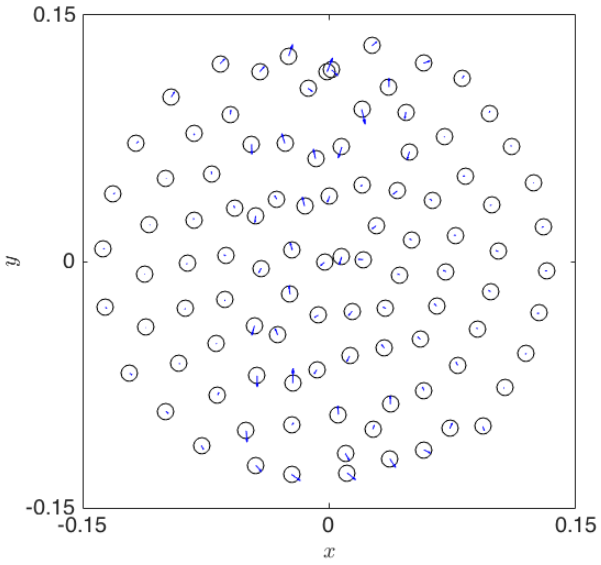

Figure 4.16: The Particle Positions and Their Velocities Corresponding to the First POD Eigenmode for $\lambda = 5$.

The percent of energy that each mode i contributes to the total energy of the system is

$$\frac{\sigma_i}{\sum_i \sigma_i} \qquad \text{where} \qquad \sigma_i = \sqrt{M}\sqrt{\gamma_i}$$

with mode one supplying the most and mode $4N$ the least.

We initialize a flock with a horizontal heading and collect the spatial and velocity data from the moment the center of mass changes horizontal direction to time 100 seconds. We perform the POD analysis described above and for each potential strength λ, at least 67% of the energy is described by mode one shown in figure 4.16. Note that the velocity components of Φ_1 are very small and all the energy of the motion is in the positional pattern of the particles.

We plot the time evolution of the coefficient A_1 given by equation (4.7) in figure 4.17. We find an exponentially damped oscillation, with stronger damping for larger λ. Since the velocity components of Φ_1 are almost zero, the oscillation of the amplitude A_1 corresponds to a periodic scaling of the corresponding particle pattern creating a pulsating swarm.

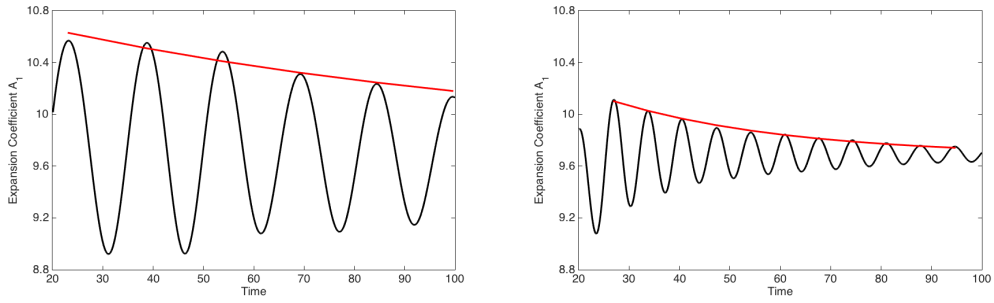

(a) $\lambda = 5$ (b) $\lambda = 25$

Figure 4.17: Time Evolution of the Projection of the Data onto the First POD Eigenmode. a) Small λ and b) larger λ.

4.3 Swarm Scattering

We conclude our analysis of swarm scattering by looking at the interaction between two flocks that collide with each other. We prepare two initial flocks satisfying Definition 1 as equilibrium solutions of the particle system (2.9) with initial velocity directions $\theta_0 \in [0, \pi/2)$ positioned far enough apart that they do not interact with each other. We arrange the positions in such a way that the two flocks moving with the velocities

$$m_L = \sqrt{\alpha/\beta}[\cos(\theta_0), \sin(\theta_0)] \qquad \text{and} \qquad m_R = \sqrt{\alpha/\beta}[-\cos(\theta_0), \sin(\theta_0)], \quad (4.8)$$

will hit each other at $x = 0$.

The parameters in this section remain the same (unless written otherwise): ratio between strength of repulsion and attraction $C = 10/9$, ratio between the length of repulsion and attraction $l = 3/4$, number of particles $N = 100$, friction force $\beta = 5$, acceleration force $\alpha = 1$, potential pre-factor $\lambda = 25$, initial heading $\theta_0 = 0$, and $\Delta t = 0.1$.

4.3.1 Two Particles

To understand the basic interaction in the Attraction-Repulsion Model we begin our analysis by a scattering of just two particles, i.e. we $N = 1$ for each flock. In this case, Eq.

(2.9) simplifies to the following eight equations:

$$\begin{aligned} \dot{x}_1 &= v_{x_1} & \dot{y}_1 &= v_{y_1} \\ \dot{x}_2 &= v_{x_2} & \dot{y}_2 &= v_{y_2} \end{aligned}$$

$$\begin{aligned} \dot{v}_{x_1} &= (\alpha - \beta(v_{x_1}^2 + v_{y_1}^2))v_{x_1} - \tfrac{x_1 - x_2}{r}\lambda U'(r) \\ \dot{v}_{y_1} &= (\alpha - \beta(v_{x_1}^2 + v_{y_1}^2))v_{y_1} - \tfrac{y_1 - y_2}{r}\lambda U'(r) \\ \dot{v}_{x_2} &= (\alpha - \beta(v_{x_2}^2 + v_{y_2}^2))v_{x_2} + \tfrac{x_1 - x_2}{r}\lambda U'(r) \\ \dot{v}_{y_2} &= (\alpha - \beta(v_{x_2}^2 + v_{y_2}^2))v_{y_2} + \tfrac{y_1 - y_2}{r}\lambda U'(r) \end{aligned} \tag{4.9}$$

where

$$r = \sqrt{(x_1 - x_2)^2 + (y_1 - y_2)^2} \quad \text{and} \quad U'(r) = (-C/l \exp[-r/l] + \exp[-r]).$$

Defining the relative distance $X = x_1 - x_2, Y = y_1 - y_2$, the relative velocity $V_x = v_{x_1} - v_{x_2}, V_y = v_{y_1} - v_{y_2}$, and the average velocity $\bar{v}_x = 1/2(v_{x_1} + v_{x_2}), \bar{v}_y = 1/2(v_{y_1} + v_{y_2})$, System (4.9) reduces to six equations

$$\begin{aligned} \dot{X} =& V_x \\ \dot{Y} =& V_y \\ \dot{V}_x =& (\alpha - \beta((\bar{v}_x + V_x/2)^2 + (\bar{v}_y + V_y/2)^2)(\bar{v}_x + V_x/2) \\ & -(\alpha - \beta((\bar{v}_x - V_x/2)^2 + (\bar{v}_y - V_y/2)^2)(\bar{v}_x - V_x/2) - 2\tfrac{X}{R}\lambda U'(R) \\ \dot{V}_y =& (\alpha - \beta((\bar{v}_x + V_x/2)^2 + (\bar{v}_y + V_y/2)^2)(\bar{v}_y + V_y/2) \\ & -(\alpha - \beta((\bar{v}_x - V_x/2)^2 + (\bar{v}_y - V_y/2)^2)(\bar{v}_y - V_y/2) - 2\tfrac{Y}{R}\lambda U'(R) \\ \dot{\bar{v}}_x =& (\alpha - \beta((\bar{v}_x + V_x/2)^2 + (\bar{v}_y + V_y/2)^2)(\bar{v}_x + V_x/2) \\ & +(\alpha - \beta((\bar{v}_x - V_x/2)^2 + (\bar{v}_y - V_y/2)^2)(\bar{v}_x - V_x/2) \\ \dot{\bar{v}}_y =& (\alpha - \beta((\bar{v}_x + V_x/2)^2)) + (\bar{v}_y + V_y/2)^2)(\bar{v}_y + V_y/2) \\ & +(\alpha - \beta((\bar{v}_x - V_x/2)^2 + (\bar{v}_y - V_y/2)^2)(\bar{v}_y - V_y/2)) \end{aligned} \tag{4.10}$$

where

$$R = \sqrt{X^2 + Y^2} \quad \text{and} \quad U'(R) = (-C/l \exp[-R/l] + \exp[-R]).$$

One-Dimensional Case

Restricting our collision to a head on collision, we start the two particles a distance μ apart on the x-axis with initial velocities $v_{x_1} = \sqrt{\alpha/\beta}, v_{x_2} = -v_{x_1}$. Thus the average velocity remain at zero for all time and System (4.10) reduces to a system of two equations where we assume without loss of generality $X > 0$

$$\begin{aligned} \dot{X} =& V_x \\ \dot{V}_x =& (\alpha - \beta(V_x^2/4))V_x - 2\lambda U'(X) \end{aligned} \tag{4.11}$$

Linearizing equation (4.11) at the steady state $(\hat{x}, 0)$ where $\hat{x}$ solves Eqn. (2.13) leads to the eigenvalues

$$\gamma_{1,2}(\alpha) = 1/2(\alpha \pm \sqrt{\alpha^2 - 8\lambda U''(\hat{x})}). \tag{4.12}$$

Since $\alpha = 1$ is set constant, our steady state is either an unstable oscillation for $\lambda > \frac{\alpha^2}{8U''(\hat{x})}$, or a saddle point. In either case, it is locally unstable.

To determine the global dynamics of the system, we analyze the nullclines of (4.11): The nullcline $\dot{X} = 0$, is given by $V_x = 0$ and

$$\begin{aligned} \dot{V}_x > 0 \quad &\text{if } X < \hat{x} \\ \dot{V}_x < 0 \quad &\text{if } X > \hat{x}. \end{aligned}$$

The nullcline where $\dot{V}_x = 0$ is given by

$$-\beta/4V_x^3 + \alpha V_x - 2\lambda U'(X) = 0, \tag{4.13}$$

We compute the discriminant of (4.13) in terms of the cubic V_x

$$\Delta_V = \beta\alpha^3 - 27/4\beta^2\lambda^2(U'(X))^2.$$

From the discriminant, we deduce that Equation (4.13) has three roots when $\Delta_V > 0$, one root when $\Delta_V < 0$, and a double root when $\Delta_V = 0$.

Lemma 1. *The steady state* $(\hat{x}, 0)$ *is unstable, if* λ *is chosen such that* $\Delta_V \geq 0$ *for all* $X \geq \hat{x}$.

Proof. For $X > \hat{x}$, the system (4.13) has two positive roots and one negative. When X passes through $\hat{x}$, one root switches from positive to negative and we see two negative roots with one positive in the interval $\hat{x} - \epsilon < X < \hat{x}$. That is, all trajectories near $\hat{x}$ on the left side of the steady state have $\dot{X} < 0$ while those near $\hat{x}$ on the right have $\dot{X} > 0$. Thus the trajectories diverge from the steady state $(\hat{x}, 0)$ (see figure 4.18). □

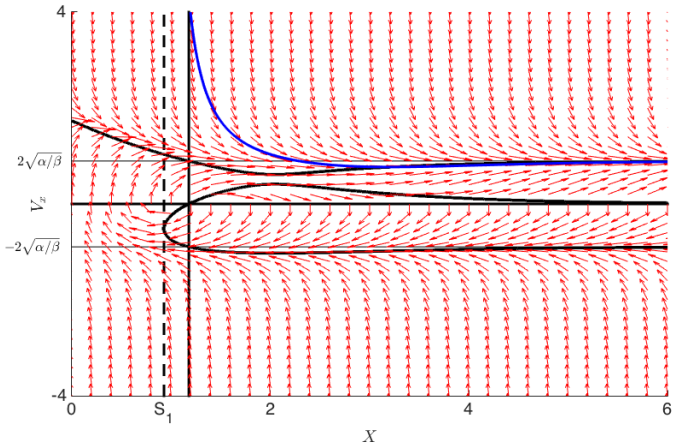

Figure 4.18: Phase Diagram for the One-Dimensional Two Particle Model Corresponding to Lemma 1: $\lambda = 5$. The steady state under question is at $V_x = 0$ and $X = \hat{x}$. We notice that no initial condition will converge to this steady state; all trajectories diverge.

Consider the case where Δ_V is not greater than zero for all $X \geq \hat{x}$. Then,

$$\Delta_V < 0 \Rightarrow \lambda > \sqrt{\frac{4\alpha^3}{27\beta(U'(X))^2}} > \sqrt{\frac{4\alpha^3}{27\beta(\max_{X \geq \hat{x}} U'(X))^2}} \tag{4.14}$$

and since $U'(X) \approx 0$ when $X \approx \hat{x}$ and X is large, Δ_V must have three double roots: S_1, S_2 and S_3 where $S_1 < \hat{x} < S_2 < S_3$ and Δ_V has

one positive root	for $0 \leq X < S_1$
one positive, two negative roots	for $S_1 < X < \hat{x}$
two positive, one negative roots	for $\hat{x} < X < S_2$
one negatie root	for $S_2 < X < S_3$
two positive, one negative roots	for $S_3 < X$

Lemma 2. *The steady state* $(\hat{x}, 0)$ *is unstable, if* λ *satisfies Eq. (4.14) and the roots* $S_2 \approx S_3$.

Proof. The proof follows similarly to Lemma 1. □

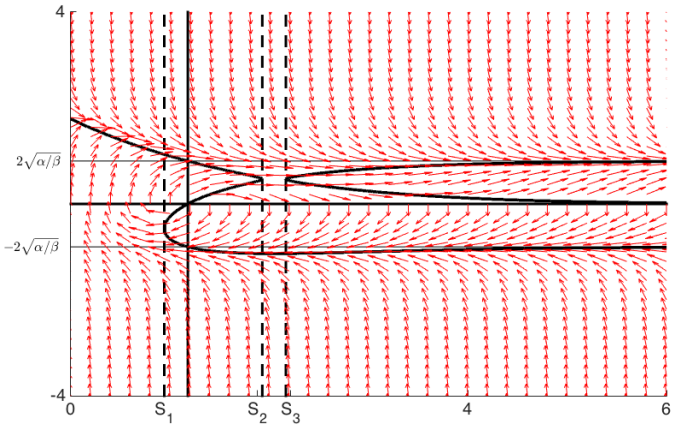

Figure 4.19: Phase Diagram for the One-Dimensional Two Particle Model Corresponding to Lemma 2: $\lambda = 5.3568$. The steady state under question is at $V_x = 0$ and $X = \hat{x}$. We notice that no initial condition will converge to this steady state; all trajectories diverge.

The following provides requirements for the stability of the steady state $(\hat{x}, 0)$ based on a large enough λ. The criteria is not optimal but provides results that there exists a λ such the trajectories of the locally unstable steady state can be trapped within a region, proving a limit cycle must exist by the Poincaré-Bendixson theorem. Our preliminary results for building the trapping region require the following Lemma:

Lemma 3. *There exists λ that satisfies Eq. (4.14) and is chosen such that*

$$\dot{V}_x \leq -2\sqrt{\alpha/\beta}$$

For

$$\hat{x} \leq X \leq \hat{x} + 1 + 2\sqrt{\alpha/\beta} \qquad \textit{and} \qquad V_x = -(X - (\hat{x} + 1 + 2\sqrt{\alpha/\beta})).$$

Proof. From Eq. (4.11)

$$\dot{V}_x = (\alpha - \beta(V_x^2/4))V_x - 2\lambda U'(X).$$

In the interval $V_x \in [0, 2\sqrt{\alpha/\beta}] \Rightarrow X \geq \hat{x} + 1$, the first term $(\alpha - \beta(V_x^2/4))V_x$ is always positive and its maximal value is given at

$$V_{\max} := \frac{2}{\sqrt{3}}\sqrt{\alpha/\beta}.$$

The second term $-2\lambda U'(X)$ is always negative. For $\dot{V}_x$ to be negative for all X and V_x in the considered intervals, we counteract term one with

$$-2\lambda \min_X(U'(X))$$

where

$$U_{\min} := \min_X(U'(X)) = U'(\hat{x} + 1 + 2\sqrt{\alpha/\beta}).$$

Solving for λ

$$\begin{aligned}(\alpha - \beta(V_{\max}^2/4))V_{\max} - 2\lambda(U_{\min}) &\leq -2\sqrt{\alpha/\beta} \\ \frac{(\alpha - \beta(V_{\max}^2/4))V_{\max} + 2\sqrt{\alpha/\beta}}{2U_{\min}} &\leq \lambda\end{aligned}$$

In the interval where $\sqrt{\alpha/\beta} \leq V_x \leq (1 + 2\sqrt{\alpha/\beta})$ and $\hat{x} \leq X < \hat{x} + 1$, term one $(\alpha - \beta(V_x^2/4))V_x$ and two $-2\lambda U'(X)$ are both negative. We will show that the same λ works for this case.

Let

$$\lambda = \frac{(\alpha - \beta(V_{\max}^2/4))V_{\max} + 2\sqrt{\alpha/\beta}}{2U_{\min}}$$

Since $V_x \geq 2\sqrt{\alpha/\beta}$, we have

$$\begin{aligned}
&(\alpha - \beta(V_x^2/4))V_x - 2\lambda U'(X) + V_x \\
&\quad = (\alpha - \beta(V_x^2/4))V_x - \lambda U'\left(\frac{V_x - 2\sqrt{\alpha/\beta}(\hat{x} + 1 + 2\sqrt{\alpha/\beta})}{2\sqrt{\alpha/\beta}}\right) + V_x \\
&\quad \leq \max_{V_x}\left[(\alpha - \beta(V_x^2/4))V_x - \lambda U'\left(\frac{V_x - 2\sqrt{\alpha/\beta}(\hat{x} + 1 + 2\sqrt{\alpha/\beta})}{2\sqrt{\alpha/\beta}}\right) + V_x\right] \\
&\quad \leq 0
\end{aligned}$$

Indeed, the last inequality gives us an even more helpful bound.

$$\dot{V}_x \leq -V_x \tag{4.15}$$

which holds for $\sqrt{\alpha/\beta} \leq V_x \leq (1 + 2\sqrt{\alpha/\beta})$ on the line $V_x = -(X - (\hat{x} + 1 + 2\sqrt{\alpha/\beta}))$.

□

Using Lemma 3, we can prove that there exists a limit cycle for a large enough λ.

Proposition 1. *The steady state $(\hat{x}, 0)$ is stable, if λ is chosen such that*

$$\dot{V}_x \leq -2\sqrt{\alpha/\beta}$$

For

$$\hat{x} \leq X \leq \hat{x} + 1 + 2\sqrt{\alpha/\beta} \qquad \textit{and} \qquad V_x = -(X - (\hat{x} + 1 + 2\sqrt{\alpha/\beta})).$$

Proof. Likewise to Lemma 1 and 2, trajectories diverge from the steady state $(\hat{x}, 0)$.

By Lemma 3, all trajectories for $\hat{x} \leq X \leq \hat{x} + 1 + 2\sqrt{\alpha/\beta}$ remain within the region under the line $V_x = -(X - (\hat{x} + 1 + 2\sqrt{\alpha/\beta}))$.

All initial values with $V_x < 0$, $\dot{X} < 0$. We connect the line $V_x = -(X - (\hat{x} + 1 + 2\sqrt{\alpha/\beta}))$ at $V_x = 0$ with a vertical line extending until we pass the single negative nullcline

vicinity. We connect this point with a horizontal line until we reach $X = 0$ where we again extend vertically until we pass the single positive nullcline in this vicinity.

At the wall $X = 0$ and $V_x > 0$, $\dot{X} > 0$ and $\dot{V} < 0$ since we are above the nullcline. The nullcline has a steady declining slope. We calculate the minimal slope of this nullcline using Eq. (4.13) with $X < \hat{x}$ and construct a linear line connecting a point above the nullcline to $V_x = -(X - (\hat{x} + 1 + 2\sqrt{\alpha/\beta}))$ at $X = \hat{x}$ and the linear line has a slope equal to the minimal slope of the nullcline. Since all trajectories approach the slope of the nullcline and we consider a line slightly above the nullcline, all trajectories remain below our constructed line.

The existence of a limit cycle directly results from applying Poincaré-Bendixson theorem. □

We provide a phase diagram for Proposition 1 in figure 4.20a). Between root S_2 and S_3, there is a separatrix where all initial conditions to the left of the separatrix approach the nullcline between S_2 and S_3 and converge to the limit cycle and those to the left diverge. We numerically compute the relative distance where trajectories start to diverge by solving the system for an initial relative velocity of $2\sqrt{\alpha/\beta}$. These values are numerically computed in figure 4.20b) where we show the separation between relative distances that converge and diverge. All trajectories are divergent for $\lambda < 9$. We see that the relative distance between converging and diverging solutions increases as λ increases, showing that the steady state $(\hat{x}, 0)$ is stable for larger λ as discussed in our analysis.

We will like to note that as seen in figure 4.20b), Lemma 3 does not find the minimal λ value. Finding this optimal λ is not trivial as seen in figure 4.21 since the limit cycle at the optimal λ will be infinitely long in the X direction. Finding a trapping region will not work. We leave this to future endeavors.

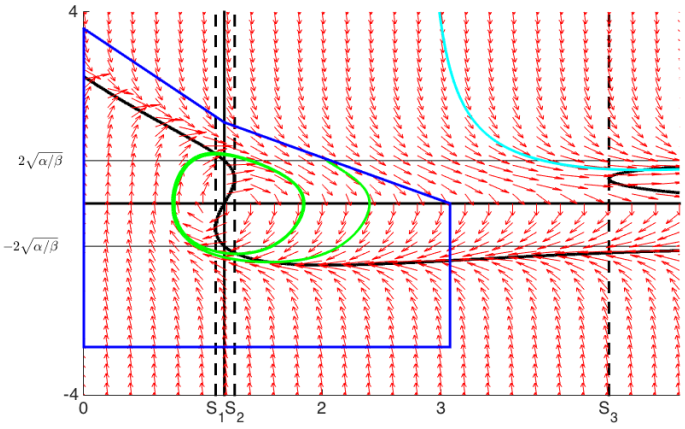

(a) Phase Diagram: $\lambda = 21.4495$

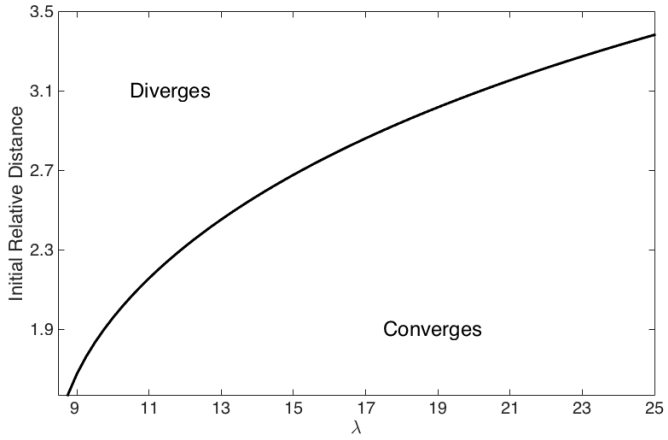

(b) Converging and Diverging Initial Conditions

Figure 4.20: Phase Diagram for the One-Dimensional Two Particle Model Corresponding to Stability Lemma 1: $\lambda = 21.4495$. a) Converging (green) and diverging (cyan) trajectories: All trajectories within the trapping region (blue) remain and converge to the limit cycle. Between the converging and diverging trajectories is a separatrix that we numerically compute in b). b) We initialize the system with an increasing relative distance and a set relative velocity $2\sqrt{\alpha/\beta}$. Running model (4.11) numerically, we find the relative distance where the trajectories start to diverge and plot the value. Any distance less than this critical relative distance will converge.

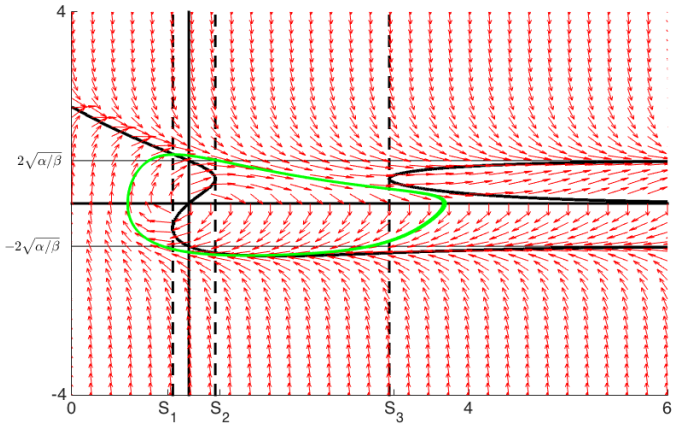

Figure 4.21: Phase Diagram for the One-Dimensional Two Particle Model with Limit Cycle Approaching the Nullcline. We set $\lambda = 8.6$ and initial relative distance $\mu = 1.4791$

Two Particles (Two-Dimensional)

We consider two particles starting a distance of μ on the x-axis with initial velocities

$$v_{x_1} = -v_{x_2} \qquad \text{and} \qquad v_{y_1} = v_{y_2}.$$

Notice that the relative distance and the relative velocity in the y direction are both zero, giving $V_y = 0$ and $Y = 0$ for all time. The average velocity in the x-direction $\bar{v}_x$ is also zero for all time since $v_{x_1} = -v_{x_2}$ and both particles undergo the same dynamics.

System (4.10) then reduces to three differential equations

$$\begin{aligned}
\dot{X} =& V_x \\
\dot{V}_x =& (\alpha - \beta(V_x^2/4 + \bar{v}_y^2))(V_x/2) + (\alpha - \beta(V_x^2/4 + \bar{v}_y^2))(V_x/2) - 2\tfrac{X_1}{|X_1|}\lambda U'(|X_1|) \\
\dot{\bar{v}}_y =& 1/2[(\alpha - \beta(V_x^2/4 + \bar{v}_y^2))\bar{v}_y + (\alpha - \beta(V_x^2/4 + \bar{v}_y^2))\bar{v}_y].
\end{aligned} \tag{4.16}$$

Setting $V = 2V_x$ and dropping the tilde for convenience, we rephrase system (4.16) in polar terms where $r^2 = V^2 + \bar{v}_y^2$ and $\zeta = \tan(\bar{v}_y/V)$:

$$\begin{aligned}
\dot{X} =& 2r\cos(\zeta) \\
\dot{r} =& r(\alpha - \beta r^2) - \lambda U'(X)\cos(\zeta) \\
\dot{\zeta} =& 1/r\lambda U'(X)\sin(\zeta)
\end{aligned} \tag{4.17}$$

Linearizing around the steady state $(X_1, r, \zeta) = (\hat{x}, \sqrt{\alpha/\beta}, \pi/2)$, we find that it has one negative real eigenvalue associated to r and two purely imaginary eigenvalues associated to X and ζ. Performing a center manifold reduction we find that r is of at least order two, leaving

$$\begin{aligned} \dot{X} =& 0 \\ \dot{\zeta} =& \tfrac{\lambda}{2}\sqrt{\beta/\alpha}U'''(\hat{x})X^2 \end{aligned} \tag{4.18}$$

as the leading order terms on the CM. We see that the origin (the fixed point) is attracting. However, the attraction is quadratic and hence very weak and the system will take very long to settle.

The determine the scattering for arbitrary initial conditions we study system (4.16) numerically for $\alpha = 1, \beta = 5$ and various initial angles $\theta_0 > 0$ and for different λ. We set the initial relative distance $X_0 = 2$ units apart and we initially set

$$\begin{aligned} V_{x_0} &= v_{x1_0} - v_{x2_0} = \cos(\pi - \theta_0) - \cos(\theta_0) = -2\cos\theta_0 \\ \bar{v}_{y_0} &= \frac{1}{2}(v_{x1_0} + v_{x2_0}) = \sin(\theta_0). \end{aligned}$$

We run the simulation for 500 time units using ode45 and compute the average velocity in the y-direction $\bar{v}_y$ after the collision (figure 4.22).

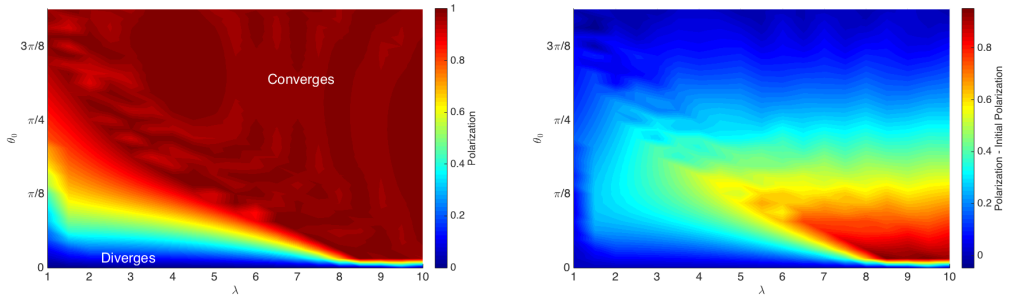

(a) Average Velocity $\bar{v}_y$ (b) Change in Average Velocity: $\bar{v}_y - \bar{v}_{y_0}$

Figure 4.22: Average Velocity $\bar{v}_y$ After the Collision of Two Interacting Particles with Various Initial Headings θ_0 and Potential Pre-Factors λ. a) Average velocity $\bar{v}_y$. b) Change in average velocity: final average velocity $\bar{v}_y$ minus initial average velocity $\bar{v}_{y_0}$.

Our results match nicely to those analyzed in section 4.2.1. For small λ, the two particles do not have enough influence on each other to change the trajectory of both particles. As a result, they just pass each other and continue on their track. As λ increases, the potential gains enough strength to capture the two particles which then oscillate around a common heading. For almost head on collisions θ_0 small, the velocity in the x-direction is transferred to a velocity in the y-direction. As discussed, that oscillation decays algebraically until both particles move in parallel straight lines.

4.3.2 Interacting Flocks

Extending the observations made in the two particle system, we consider the full N particle system Eq. (2.9). We initially set the center of mass of the left flock at the origin and the center of mass of the right flock at position $(5, 0)$. The velocities are given by Eq. 4.8 with $\theta_0 \in [0, \pi/2)$.

As in the previous sections, we analyze the behavior of the system after the collision as a function of the potential pre-factor λ and the collision angles θ_0. Three observables are used to characterize the collective behavior over time t: Polarization $P(t)$, Angular Momentum $M(t)$, and Absolute Angular Momentum $M_{abs}(t)$ defined as:

$$P(t) = \left| \frac{\sum_i v_i(t)}{\sum_i |v_i(t)|} \right| \tag{4.19}$$

$$M(t) = \left| \frac{\sum_i r_i(t) \times v_i(t)}{\sum_i |r_i||v_i|} \right| \tag{4.20}$$

$$M_{\text{abs}}(t) = \left| \frac{\sum_i |r_i(t) \times v_i(t)|}{\sum_i |r_i||v_i|} \right| \tag{4.21}$$

where $r_i(t) = x_i(t) - x_{cm}(t)$ with $x_{cm}(t)$ the position of the center of mass at time t. We will not distinguish between double mills and mills so our analysis does not include angular momentum $M(t)$.

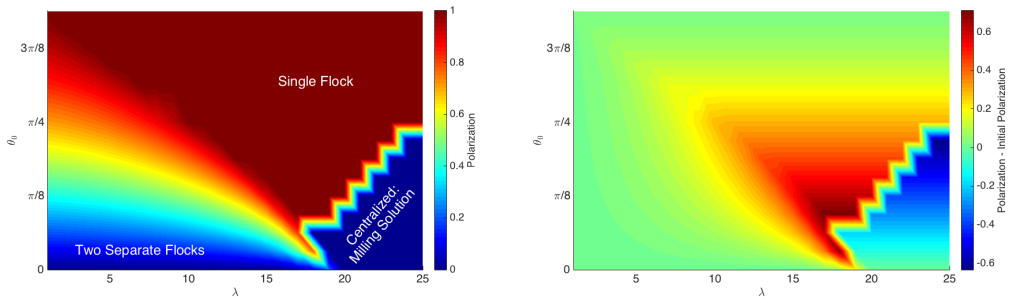

(a) Poloarization (b) Change in Polarization: Final - Initial

Figure 4.23: Polarization After the Collision of Two Interacting Flocks. a) Polarization. b) Change in polarization: final polarization minus initial polarization. We run the simulation for 500 time units and average over the last 50 time units of the simulation.

For both mills and double mills, Polarization $P \approx 0$ while Absolute Angular Momentum $M_{\text{abs}} \approx 1$. Systems that settle into a flocking state will have high Polarization $P \approx 1$ and $M_{\text{abs}} \approx 0$. Similarly seen in the two particle system, some flocks will fail to merge but the interaction makes them alter their initial heading. $P > 0$ and M_{abs} is small.

For various initial angles θ_0 and potential pre-factors, we provide P of the flocks in figure 4.23. We do not provide Absolute Angular Momentum M_{abs} since we can deduce where $M_{\text{abs}} \approx 1$ from the Polarization plot.

The results are very similar to the scattering of two particles: For weak potential (i.e. small λ), the two flocks just pass each other and diverge. The interaction results in a small change of the departing angles towards each other but the change is not big enough to merge the two flocks. As λ increases we find convergence of the two flocks: For large λ and glancing collisions θ_0 large, the two flocks merge and move as a single flock with uniform velocity. For large λ and head-on collisions, the two flocks merge and generate a *bound state* in the form of a milling solution. The transition region between the two states show unpredictable and complicated behavior - in addition to the milling solution, double mills and disintegrating flocks can be found.

4.4 Discussion

We studied the Attraction-Repulsion Model by numerically simulating the how the flock impacts a flat, reflecting surface. In addition, we analyzed the equations of motion for two particles colliding under the influence of the attraction-repulsion potential and extended our observations to the corresponding scattering for two colliding flocks. In both cases we found that the strength of the potential determined the degree of inelastic scattering displayed by the flock.

In wall scattering, the inelastic behavior manifested itself by an excitation of internal swarm oscillations when the flock left the boundary. We used a Proper Orthogonal Decomposition analysis to determine the dominant mode of the oscillation that led to an oscillatory scaling of the swarm structure akin to a breathing motion. In addition, inelastic scattering prompted a stickiness to the wall, producing a refraction law that tilted towards a motion of the flock aligning to the wall. As a result, we derived a refraction map that related incoming and outgoing angles of the swarm and showed that the behavior of a swarm in a channel and in a square could be understood as the stable and unstable fixed points of the iterated refraction map. In a channel, the attractor was a motion parallel to the channel.

In a square, there was a bifurcation from motion parallel to the boundary that transitioned to a rotating motion. The bifurcation was degenerate in the sense that near the critical potential strength, there existed continua of periodic orbits (i.e. fixed points of the refraction map) that were neutrally stable. Comparing the iterated maps with actual flock simulations, we found perfect agreement. For both weak and strong potentials, the swarms aligned with the wall directions and rotated on a periodic trajectory, respectively. However, for potential strength close to the degenerate bifurcation of the map, the dynamics became more complicated. Since the interaction with the wall introduced noise, individual particles might split off from the flock which might eventually lead to a complete disintegration of

the flock that never reformed. Alternatively, the noise allowed the trajectories of the center of mass of the swarm to explore the neutrally stable periodic orbits randomly, including switching rotational direction. The latter phenomenon also occurred in the channel, where for weaker potentials the flock moved transversally to the channel, drifting randomly along the channel axis but never converging to a motion parallel to the channel.

The scattering of two colliding particles became a four-dimensional dynamical system that could be understood analytically. The solutions either scattered away from each other or converged to periodically damped orbits where the particles converged and particles eventually adapted a like heading. When performing numerical simulations of the collisional dynamics, two colliding flocks showed the same type of behavior. If the ratio of kinetic energy to potential energy was large, the paths of the two flocks crossed, the angle between the two velocity vectors decreased, but the two flocks still diverged. As the potential energy increased, the two flocks converged to a common direction until, for large enough potential energy, a bounded state appeared in the form of a milling solution.

Chapter 5

CONCLUSIONS

We study self-propelled particle mathematical models where agents interact and evolve according to behavioral rules that lead to swarming behavior. Starting from the canonical model of Reynolds (1987) who define three interaction zones by attraction, repulsion, and alignment, two simplified models have received a lot of attention: An attraction-repulsion model, eliminating alignment, is proposed by D'Orsogna *et al.* (2006) while Vicsek *et al.* (1995) show that the minimal requirement for collective motion is alignment and consider a model with only alignment.

Most theoretical work on these models has been concerned with swarm solutions in infinite domains and focus on the bifurcations from disorganized to organized motion. This thesis provides numerical simulations and develops understandings of swarms in finite domains.

By restricting the Vicsek Model to finite domains, we overcome one of its shortcomings: Aggregating organisms generally possess spatial coherence along with a common directional movement. The members in the Vicsek Model disperse in space Vicsek *et al.* (1995). While this can be remedied with an attraction force, (Grégoire and Chaté (2004) and Chaté *et al.* (2008)), the additional attraction term is cumbersome and takes away from the simplistic nature of the model. We show, however, that in bounded domains the Vicsek Model generates swarms that have spatial coherence without the aid of attraction forces. In doing so, the boundaries possess a type of stickiness that leads to new types of collective motion in addition to the single vortex discovered by Czirók and Vicsek (2000).

Specifically, in a channel domain we find periodic wavelike motions with oscillatory behavior between boundary layers where particles are densely aggregated near the channel

walls. We show how the period of the wave depends on the noise level and the influence horizon. In a disk and a square domain, we find single rotating swarms. The trajectories of the center of mass break the $O(2)$ symmetry of the disk to an $SO(2)$ symmetry, and similarly, the D^4 symmetry of the square is broken to a C^4 symmetry. We find that the averaged flow is stationary in the form of a single vortex (mill solution) independent of the initial transient behavior of the swarm. When the average velocity is small, the single vortex disappears and the center of mass of the swarm begins to behave chaotically for systems with small noise.

The Attraction-Repulsion Model by D'Orsogna *et al.* (2006) also has spatial limitations. The translationally invariant flock steady state is defined with particles within a finite distance of each other, but the flock is not centrally localized and explores all space. Because most animals remain near a preferred location that provides food, shelter, etc., Carrillo *et al.* (2010) introduce a roosting force to the model, limiting its translational region. The roosting force allows for new behavior like milling flocks and double milling flocks. Again, a bounded domain with specularly reflecting walls leads to spatially localized behavior without the need of additional forces.

To understand the swarm-wall interaction for the Attraction-Repulsion Model, we study a single wall impact of the flock when the flock's members are specularly reflected at the wall. We find that the collision is inelastic and derive the refraction law for the outgoing angle of a flock as a function of the incoming angle and the strength of the potential force. For flocks that are dominated by kinetic energy, the flock as a whole reflects specularly. As the potential energy increases, the interaction becomes inelastic and internal pulsations of the swarm are generated that decay exponentially.

Using the refraction law as a one-dimensional map, we can iterate the map and predict the dynamics of a flock subject to multiple wall interactions. In a channel the iterated map shows an attracting fixed point corresponding to a motion aligned with the channel sides.

This is confirmed for large potential forces in the actual agent simulations. For weak noise and small potential forces, however, the flock bounces between the channel walls drifting randomly along the channel but never converging to a motion aligned with the channel.

For a square domain, the refraction law map predicts a degenerate bifurcation at a critical potential strength. At higher potential strengths, the trajectory of the iterated map follows a C^4 symmetric path where a single attracting fixed point of the map is seen. This path breaks to a C^2 symmetry with a band of neutrally stable fixed points when the strength decreases. The symmetry breaks altogether at lower strengths and the rotation frequently changes direction with no directional preference. The degenerate bifurcation corresponds to specular reflection of the swarm where every incoming angle of the flock results in a periodic orbit. Any strengths below this transition produce unstable rotational fixed points and the trajectory approaches and remains near a path parallel to the boundary. The flock set in a square domain behaves similarly with the single attracting fixed point occurring for larger potential strengths and near the bifurcation point, the flock breaks apart due to the continual noise contribution.

An extension to the wall scattering experiments is the collision of two identical flocks. Beginning with the collision of two particles, we show that at lower potential strengths, the two particles weakly interact and continue on their initial path with a slight reduction in the difference between the outgoing angles. Increasing the potential strength leads to bound states: Particles are caught in a damped period orbit that merges very slowly to two particles moving parallel in the same direction. For head on collisions, the two particles will have no net movement and produce an oscillating behavior.

Scaling up to full flocks colliding, we find qualitatively the same transition between scattered and bound states. However, the head on oscillation acquires a larger basin of attraction and leads to bounded states of mill type flows.

5.1 Future Work

Our current work provides insight to how reflecting boundaries alter the dynamical nature of two well-studied SPP Models. As illustrated in chapter 3, boundaries become sticky but, nevertheless, particles slip by the boundary.

To motivate more realistic boundary conditions for hydrodynamic macroscopic models, we refer to the sticky boundary layer in channel flow and to observations in fluid dynamics. Perfect, frictionless fluids follow differential equations of motion proposed by Euler. D'Alembert, however, uses the Euler equations to prove that inviscid and irrotational flow slips along the contour of the boundary with no drag force or lift from the boundary, contradicting experimental results and leading to the famous D'Alembert Paradox. Fluid flows experience some, if not, a substantial drag or lift from the boundary.

In 1904, Prandtl hypothesizes that fluids close to the wall surface interact with wall atoms and, in consequence, slow down dramatically to an average of zero. A chain reaction occurs where these hardly moving particles influence neighboring particles and this interaction reduces the average speed; the velocity profiles monotonically increases away from the boundary. Prandtl points out that fluid flows with small viscosity can be divided into a boundary layer near the wall where the effects of viscosity are significant and a nearly inviscid outer layer that connects smoothly the the boundary layer and satisfies the Euler equations. Boundary-layer theory has proven to be useful and has given fluid flow a boost in theoretical analysis instead of relying solely on experiments.

We argue that a similar reduction in average velocity is present for collectively moving organisms. Examples include a flock of birds that avoids buildings when flying near the ground or a cattle drive moving against a fence where the uneven friction and the cows constant pushing causes the herd to slow near the fence.

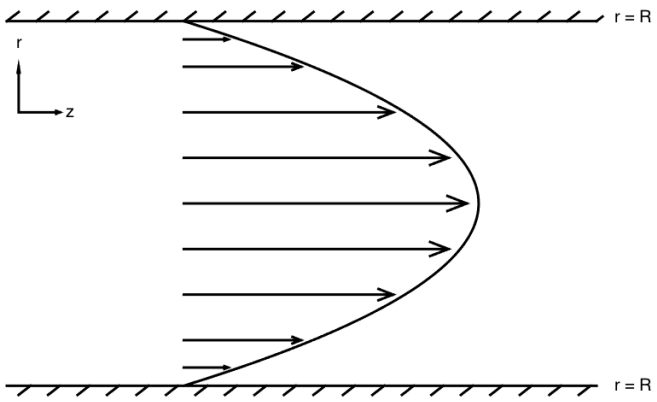

Figure 5.1: Poiseuille's Flow in a Channel: Parabolic Velocity Profile.

Developing a comparison to the already theorized boundary-layer theory applied to fluid dynamics, we will consider the continuous-time Vicsek Model near a boundary at $x = 0$ and $x = L$ where L is the width of the channel and x the coordinate normal to the boundary. Explicitly, the model is the same as in Eq. (2.6) with a Brownian motion term of the form $\sqrt{2\hat{d}}\, dB_t$.

The parameter $\hat{d} \geq d$ is a function of the noise level d and position x. In free space, $\hat{d} = d$ while $\hat{d}$ monotonically increases as x approaches the boundary. The particles closest to the boundary are dominated by the noise term and do not move on average while those further from the wall follow the velocity distribution determined by the von Mises Distribution Eq. (3.2).

Introducing a boundary roughness in the particle models, we plan to compare the microscopic Vicsek Model and the hydrodynamic macroscopic Vicsek Model with no-slip boundary conditions. The goal is to develop a boundary layer theory similar to the one in Schlichting *et al.* (2000) for Poiseuille's flow in a channel (figure 5.1.)

Another idea is borrowed from the concept of Brownian motors. Brownian motors generate directed motion from interaction with noise by exploiting coherence properties of the noise. They are considered the drivers of bacteria and nanoparticles in noisy environments.

A typical experiment involves a set of particles subject to Brownian motion in a asymmetric channel as seen in figure 5.2. Assuming an external field dragging particles down a potential slope, Astumian and Hänggi (2002) and Reimann and Hänggi (2002) show that with strong enough Brownian motion, the net motion of the particles is moving against the potential slope.

To illustrate a typical argument supporting the previous claim, Astumian and Hänggi (2002) concentrate all particles at the bottom of a potential well at x_0 (see figure 5.3 (top)). As the sawtooth potential strength periodically oscillates, the potential weakens and the probability distribution diffuses as a Gaussian as seen in figure 5.3 (middle) where it extends over the well positions x_0, $x_0 + L_1$ and $x_0 - L_2$. When the sawtooth potential is applied again, the probability distribution that particles are caught in one of the three basins is shown in figure 5.3 (bottom). Since $L_1 > L_2$, the probability of finding a particle in $x_0 - L_2$ is higher than in $x_0 + L_1$ and thus the particles gain a net transport against the potential gradient.

Nobody, thus far, has studied self-propelled particles in this context. Assuming Vicsek particles in their diffusive state, they are really governed by Brownian motion and hence should show the same effects as a Brownian motor, Hänggi *et al.* (2005). Once a swarm forms, the system is no longer a Brownian motor but the interaction with a boundary will still lead to spatial coherence near the boundary with random diffusion in space and a von Mises distribution on the velocity in the middle of the channel. It will be interesting to see whether such ideas can be used to steer and control the motion of Vicsek swarms.

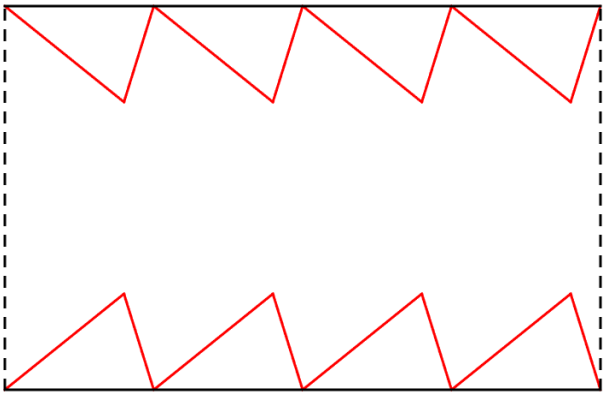

Figure 5.2: Channel with Sawtooth Edges: the x Direction Remains Periodic and the Sawtooth Edges Reflect Specularly.

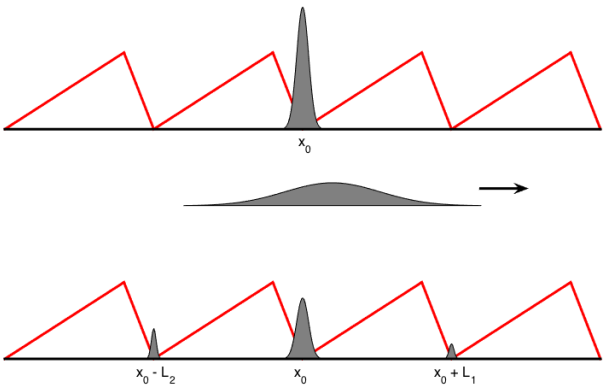

Figure 5.3: Particle Probability Distribution in a Sawtooth Channel. (top) All particles initially concentrated at the position x_0. (middle) Sawtooth potential is turned off and the particles move left due to the force, but also diffuse evenly left and right. A Gaussian probability is seen. (bottom) Sawtooth potential is turned on and the particle is trapped at the bottom of a well. From the Gaussian distribution (middle), the particle is more likely in the left well than the right.

REFERENCES

Aoki, I., "A simulation study on the schooling mechanism in fish.", Bulletin of The Japanese Society of Fisheries Science **48**, 8, 1081–1088 (1982).

Astumian, R. D. and P. Hänggi, "Brownian motors", (2002).

Attanasi, A., A. Cavagna, L. Del Castello, I. Giardina, S. Melillo, L. Parisi, O. Pohl, B. Rossaro, E. Shen, E. Silvestri *et al.*, "Collective behaviour without collective order in wild swarms of midges", (2014).

Ballerini, M., N. Cabibbo, R. Candelier, A. Cavagna, E. Cisbani, I. Giardina, V. Lecomte, A. Orlandi, G. Parisi, A. Procaccini *et al.*, "Interaction ruling animal collective behavior depends on topological rather than metric distance: Evidence from a field study", Proceedings of the national academy of sciences **105**, 4, 1232–1237 (2008).

Bazazi, S., C. C. Ioannou, S. J. Simpson, G. A. Sword, C. J. Torney, P. D. Lorch and I. D. Couzin, "The social context of cannibalism in migratory bands of the mormon cricket", PloS one **5**, 12, e15118–e15118 (2010).

Bode, N. W., D. W. Franks and A. J. Wood, "Limited interactions in flocks: relating model simulations to empirical data", Journal of The Royal Society Interface p. rsif20100397 (2010).

Buhl, J., D. J. Sumpter, I. D. Couzin, J. J. Hale, E. Despland, E. Miller and S. J. Simpson, "From disorder to order in marching locusts", Science **312**, 5778, 1402–1406 (2006).

Buhl, J., G. A. Sword and S. J. Simpson, "Using field data to test locust migratory band collective movement models", Interface Focus p. rsfs20120024 (2012).

Carrillo, J., M. D'orsogna and V. Panferov, "Double milling in self-propelled swarms from kinetic theory", Kinetic and Related Models **2**, 2, 363–378 (2009).

Carrillo, J., Y. Huang and S. Martin, "Nonlinear stability of flock solutions in second-order swarming models", Nonlinear Analysis: Real World Applications **17**, 332–343 (2014a).

Carrillo, J., S. Martin and V. Panferov, "A new interaction potential for swarming models", Physica D: Nonlinear Phenomena **260**, 112–126 (2013).

Carrillo, J. A., Y. Huang and S. Martin, "Explicit flock solutions for quasi-morse potentials", European Journal of Applied Mathematics **25**, 05, 553–578 (2014b).

Carrillo, J. A., A. Klar, S. Martin and S. Tiwari, "Self-propelled interacting particle systems with roosting force", Mathematical Models and Methods in Applied Sciences **20**, supp01, 1533–1552 (2010).

Cavagna, A., A. Cimarelli, I. Giardina, A. Orlandi, G. Parisi, A. Procaccini, R. Santagati and F. Stefanini, "New statistical tools for analyzing the structure of animal groups", Mathematical biosciences **214**, 1, 32–37 (2008a).

Cavagna, A., I. Giardina, A. Orlandi, G. Parisi and A. Procaccini, "The starflag handbook on collective animal behaviour: 2. three-dimensional analysis", Animal Behaviour **76**, 1, 237–248 (2008b).

Cavagna, A., I. Giardina, A. Orlandi, G. Parisi, A. Procaccini, M. Viale and V. Zdravkovic, "The starflag handbook on collective animal behaviour: 1. empirical methods", Animal Behaviour **76**, 1, 217–236 (2008c).

Chaté, H., F. Ginelli, G. Grégoire, F. Peruani and F. Raynaud, "Modeling collective motion: variations on the vicsek model", The European Physical Journal B **64**, 3-4, 451–456 (2008).

Chuang, Y.-l., M. R. D'orsogna, D. Marthaler, A. L. Bertozzi and L. S. Chayes, "State transitions and the continuum limit for a 2d interacting, self-propelled particle system", Physica D: Nonlinear Phenomena **232**, 1, 33–47 (2007).

Couzin, I. D., J. Krause, R. James, G. D. Ruxton and N. R. Franks, "Collective memory and spatial sorting in animal groups", Journal of theoretical biology **218**, 1, 1–11 (2002).

Cucker, F. and E. Mordecki, "Flocking in noisy environments", Journal de mathématiques pures et appliquées **89**, 3, 278–296 (2008).

Cucker, F. and S. Smale, "Emergent behavior in flocks", Automatic Control, IEEE Transactions on **52**, 5, 852–862 (2007).

Czirók, A., A.-L. Barabási and T. Vicsek, "Collective motion of self-propelled particles: Kinetic phase transition in one dimension", Physical Review Letters **82**, 1, 209 (1999).

Czirók, A. and T. Vicsek, "Collective behavior of interacting self-propelled particles", Physica A: Statistical Mechanics and its Applications **281**, 1, 17–29 (2000).

Degond, P., J.-G. Liu, S. Motsch and V. Panferov, "Hydrodynamic models of self-organized dynamics: derivation and existence theory", arXiv preprint arXiv:1108.3160 (2011).

Degond, P. and S. Motsch, "Continuum limit of self-driven particles with orientation interaction", Mathematical Models and Methods in Applied Sciences **18**, supp01, 1193–1215 (2008a).

Degond, P. and S. Motsch, "Large scale dynamics of the persistent turning walker model of fish behavior", Journal of Statistical Physics **131**, 6, 989–1021 (2008b).

Degond, P. and T. Yang, "Diffusion in a continuum model of self-propelled particles with alignment interaction", Mathematical Models and Methods in Applied Sciences **20**, supp01, 1459–1490 (2010).

Degond, P. and H. Yu, "Self-organized hydrodynamics in an annular domain: Modal analysis and nonlinear effects", Mathematical Models and Methods in Applied Sciences **25**, 03, 495–519 (2015).

DeLellis, P., G. Polverino, G. Ustuner, N. Abaid, S. Macrì, E. M. Bollt and M. Porfiri, "Collective behaviour across animal species", Scientific reports **4** (2014).

D'Orsogna, M. R., Y.-L. Chuang, A. L. Bertozzi and L. S. Chayes, "Self-propelled particles with soft-core interactions: patterns, stability, and collapse", Physical review letters **96**, 10, 104302 (2006).

Fetecau, R. C., Y. Huang and T. Kolokolnikov, "Swarm dynamics and equilibria for a nonlocal aggregation model", Nonlinearity **24**, 10, 2681 (2011).

Gajamannage, K., S. Butail, M. Porfiri and E. M. Bollt, "Dimensionality reduction of collective motion by principal manifolds", Physica D: Nonlinear Phenomena **291**, 62–73 (2015).

Gamba, I. M. and M.-J. Kang, "Global weak solutions for kolmogorov-vicsek type equations with orientational interaction", arXiv preprint arXiv:1502.00293 (2015).

Gautrais, J., C. Jost, M. Soria, A. Campo, S. Motsch, R. Fournier, S. Blanco and G. Theraulaz, "Analyzing fish movement as a persistent turning walker", Journal of mathematical biology **58**, 3, 429–445 (2009).

Gazi, V. and K. M. Passino, "Stability analysis of swarms in an environment with an attractant/repellent profile", in "American Control Conference, 2002. Proceedings of the 2002", vol. 3, pp. 1819–1824 (IEEE, 2002).

Gazi, V. and K. M. Passino, "A class of attractions/repulsion functions for stable swarm aggregations", International Journal of Control **77**, 18, 1567–1579 (2004).

Grégoire, G. and H. Chaté, "Onset of collective and cohesive motion", Physical review letters **92**, 2, 025702 (2004).

Grossman, D., I. Aranson and E. B. Jacob, "Emergence of agent swarm migration and vortex formation through inelastic collisions", New Journal of Physics **10**, 2, 023036 (2008).

Ha, S.-Y., K. Lee, D. Levy *et al.*, "Emergence of time-asymptotic flocking in a stochastic cucker-smale system", Communications in Mathematical Sciences **7**, 2, 453–469 (2009).

Handegard, N. O., K. M. Boswell, C. C. Ioannou, S. P. Leblanc, D. B. Tjøstheim and I. D. Couzin, "The dynamics of coordinated group hunting and collective information transfer among schooling prey", Current biology **22**, 13, 1213–1217 (2012).

Hänggi, P., F. Marchesoni and F. Nori, "Brownian motors", Annalen der Physik **14**, 1-3, 51–70 (2005).

Hemelrijk, C. K. and H. Kunz, "Density distribution and size sorting in fish schools: an individual-based model", Behavioral Ecology **16**, 1, 178–187 (2005).

Herbert-Read, J. E., A. Perna, R. P. Mann, T. M. Schaerf, D. J. Sumpter and A. J. Ward, "Inferring the rules of interaction of shoaling fish", Proceedings of the National Academy of Sciences **108**, 46, 18726–18731 (2011).

Huth, A. and C. Wissel, "The simulation of the movement of fish schools", Journal of theoretical biology **156**, 3, 365–385 (1992).

Katz, Y., K. Tunstrøm, C. C. Ioannou, C. Huepe and I. D. Couzin, "Inferring the structure and dynamics of interactions in schooling fish", Proceedings of the National Academy of Sciences **108**, 46, 18720–18725 (2011).

Kelley, D. H. and N. T. Ouellette, "Emergent dynamics of laboratory insect swarms", Scientific reports **3** (2013).

Kirby, M., *Geometric data analysis: an empirical approach to dimensionality reduction and the study of patterns* (John Wiley & Sons, Inc., 2000).

Levine, H., W.-J. Rappel and I. Cohen, "Self-organization in systems of self-propelled particles", Physical Review E **63**, 1, 017101 (2000).

Lin, Y. and N. Abaid, "Collective behavior and predation success in a predator-prey model inspired by hunting bats", Physical Review E **88**, 6, 062724 (2013).

Lukeman, R., Y.-X. Li and L. Edelstein-Keshet, "Inferring individual rules from collective behavior", Proceedings of the National Academy of Sciences **107**, 28, 12576–12580 (2010).

Mikhailov, A. S. and D. H. Zanette, "Noise-induced breakdown of coherent collective motion in swarms", Physical Review E **60**, 4, 4571 (1999).

Miller, P. W. and N. T. Ouellette, "Impact fragmentation of model flocks", Physical Review E **89**, 4, 042806 (2014).

Mogilner, A., L. Edelstein-Keshet, L. Bent and A. Spiros, "Mutual interactions, potentials, and individual distance in a social aggregation", Journal of mathematical biology **47**, 4, 353–389 (2003).

Motsch, S. and L. Navoret, "Numerical simulations of a nonconservative hyperbolic system with geometric constraints describing swarming behavior", Multiscale Modeling & Simulation **9**, 3, 1253–1275 (2011).

Motsch, S. and E. Tadmor, "A new model for self-organized dynamics and its flocking behavior", Journal of Statistical Physics **144**, 5, 923–947 (2011).

Mwaffo, V., S. Butail, M. di Bernardo and M. Porfiri, "Measuring zebrafish turning rate", Zebrafish **12**, 3, 250–254 (2015).

Potiguar, F. Q., G. Farias and W. Ferreira, "Self-propelled particle transport in regular arrays of rigid asymmetric obstacles", Physical Review E **90**, 1, 012307 (2014).

Reimann, P. and P. Hänggi, "Introduction to the physics of brownian motors", Applied Physics A **75**, 2, 169–178 (2002).

Reynolds, C. W., "Flocks, herds and schools: A distributed behavioral model", in "ACM Siggraph Computer Graphics", vol. 21, pp. 25–34 (ACM, 1987).

Romanczuk, P. and L. Schimansky-Geier, "Swarming and pattern formation due to selective attraction and repulsion", Interface focus **2**, 6, 746–756 (2012).

Schlichting, H., K. Gersten and K. Gersten, *Boundary-layer theory* (Springer Science & Business Media, 2000).

Strömbom, D., "Collective motion from local attraction", Journal of theoretical biology **283**, 1, 145–151 (2011).

Sumpter, D. J., R. P. Mann and A. Perna, "The modelling cycle for collective animal behaviour", Interface Focus **2**, 6, 764–773 (2012).

Tenenbaum, J. B., V. De Silva and J. C. Langford, "A global geometric framework for nonlinear dimensionality reduction", Science **290**, 5500, 2319–2323 (2000).

Vicsek, T., A. Czirók, E. Ben-Jacob, I. Cohen and O. Shochet, "Novel type of phase transition in a system of self-driven particles", Physical review letters **75**, 6, 1226 (1995).

Vicsek, T. and A. Zafeiris, "Collective motion", Physics Reports **517**, 3, 71–140 (2012).

Zienkiewicz, A., D. A. Barton, M. Porfiri and M. di Bernardo, "Data-driven stochastic modelling of zebrafish locomotion", Journal of mathematical biology pp. 1–25 (2014).

APPENDIX A

COEFFICIENTS C_1, C_2 AND λ

Analytically derived in Degond and Motsch (2008a), the coefficients c_1 and c_2 all rely on the Von Mises Distribution $M_\Omega(\omega)$ (3.2) and c_2 also relies on the generalized collisional invariant $\psi(\theta)$ derived in Degond and Motsch (2008a). As mentioned in Motsch and Navoret (2011), the $\psi(\theta)$ is periodic in 2D and satisfies the eliptic equation:

$$\partial_\theta \left(e^{\frac{\cos\theta}{d}} \partial_\theta \psi \right) = \sin\theta e^{\frac{\cos\theta}{d}} \tag{A.1}$$

which gives us the following solution

$$\psi(\theta) = -d\theta + d\pi \frac{\int_0^\theta e^{\frac{\cos\theta}{d}}}{\int_0^\pi e^{\frac{\cos\theta}{d}}} \tag{A.2}$$

The coefficients c_1, c_2 and λ are given as where $M(\theta) = e^{\frac{\cos\theta}{d}}$, we have

$$\begin{aligned} c_1 &= \int_{-\pi}^{\pi} \cos\theta M(\cos\theta) d\theta \\ c_2 &= \frac{\int_{-\pi}^{\pi} \cos\theta \sin\theta \psi(\theta) M(\theta) d\theta}{\int_{-\pi}^{\pi} \sin\theta \psi(\theta) M(\theta) d\theta} \\ \lambda &= d \end{aligned}$$

where d is the noise parameter. Since there is no explicit expression for $\psi(\theta)$ or for the integral of $M(\theta)$, we use numerical integration to estimate c_1 and c_2 and plot c_2/c_1 and λ/c_1 in figure A.1 for different values of d.

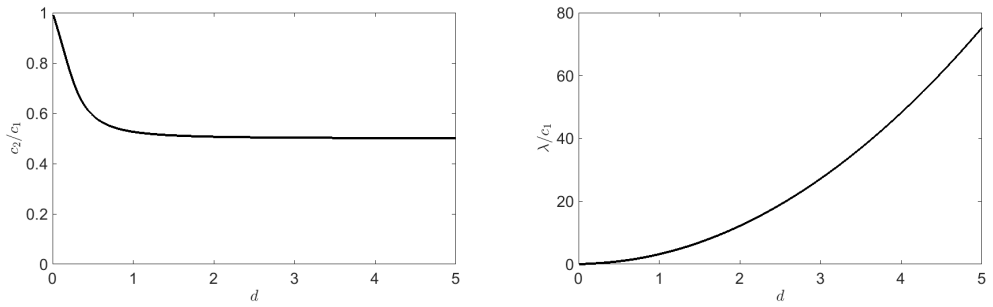

(a) $c = c_2/c_1$ (b) $\hat{\lambda} = \lambda/c_1$

Figure A.1: Parameters $c = c_2/c_1$ and $\hat{\lambda} = \lambda/c_1$ for varying noise d.

APPENDIX B

NUMERICAL DIFFICULTIES

Here, we describe the numerical difficulties that arise when numerically evaluating the attraction/repulsion model (2.9) in bounded domains.

D'Orsogna *et al.* (2006) implement the multistep, implicit Adams-Bashforth-Moulton 4th order method, written explicitly:

$$\begin{aligned} &\text{The predictor: } p_j^{(n+1)} = y_j^{(n)} + \tfrac{h}{24}(-9f^{(n-3)} + 37f^{(n-2)} - 59f^{(n-1)} + 55f_j^{(n)}) \\ &\text{The corrector: } z_j^{(n+1)} = z_j^{(n)} + \tfrac{h}{24}(f^{(n-2)} - 5f^{(n-1)} + 19f^{(n)} + 9f(p_j^{n+1})) \end{aligned} \tag{B.1}$$

where a single particle with position $z_j = (x_j, y_j)$ and velocity $v = (v_{x_j}, v_{y_j})$ in the Attraction-Repulsion Model evolves according to

$$\dot{z} = f(v) = v \qquad \text{and} \qquad \dot{v} = 0$$

since the potential has no influence (only one particle is considered) and we assume the particle has converged to the desired speed. Let the x-direction velocity $v_{x_j}^{(0)}$ reflect at time step (n) for $n > 0$. That is, $v_{x_j}^{(n)} = -v_{x_j}^{(0)}$. At time step $(n+4)$, all velocities used for the update are equal to $-v_{x_j}^{(0)}$.

To determine the path of the reflected particle, we calculate the update for $x_j^{(n+4)}$ and $y_j^{(n+4)}$ starting at position $x_j^{(n)}$ and writing the update in terms of $-v_{x_j}^{(0)}$ and $(x_j^{(n)}, x_j^{(n)})$.

$$\begin{aligned} x_j^{(n+4)} &= \tfrac{(1+3/8h)^4}{4096} x^{(n)} - \tfrac{h(1161h^4+8964h^3+30528h^2+58880h+45056)}{16384} v_{x_j}^{(0)} \\ y_j^{(n+4)} &= \tfrac{(1+3/8h)^4}{4096} y^{(n)} + \tfrac{h(81h^4+999h^3+4896h^2+11904h+10240)}{4096} v_{y_j}^{(0)} \end{aligned} \tag{B.2}$$

For the particle to reflect specularly, the coefficients of $v_{x_j}^{(0)}$ and $v_{y_j}^{(0)}$ must equal or the particle travels further in one direction along the velocity than in the other. With differing coefficients, the resulting trajectory does not to follow a specularly reflected path as the method continues with the velocity $[-v_{x_j}^{(0)}, v_{y_j}^{(0)}]$.

We choose to implement the Runge-Kutta 4th order method Eq. (B.3) instead. Since it is a one-step method that only uses one time step to update to the new time step, the particle j reflects specularly.

$$\begin{aligned} k_1 &= f(x^{(n)}, v^{(n)}) \\ k_2 &= f(x^{(n)}, v^{(n)}) \\ k_3 &= f(x^{(n)}, v^{(n)}) \\ k_4 &= f(x^{(n)}, v^{(n)}) \end{aligned} \tag{B.3}$$

$$z_j^{(n+1)} = z_j^{(n)} + \tfrac{h}{6}(k_1 + 2k_2 + 2k_3 + k_4)$$

Without this discontinuity, the Adams-Bashforth-Moulton 4th order method is the more desired method to employ since you only evaluate the function once per time step evaluation instead of four times with the Runge-Kutta. It is a much faster method.